

# Magic Numbers for Classical Lennard-Jones Cluster Heat Capacities

D. D. Frantz

*Department of Chemistry, University of Lethbridge,*

*Lethbridge, T1K 3M4, Canada*

(November 16, 2018)

## Abstract

Heat capacity curves as functions of temperature for classical atomic clusters bound by pairwise Lennard-Jones potentials were calculated for aggregate sizes  $4 \leq N \leq 24$  using Monte Carlo methods. J-walking (or jump-walking) was used to overcome convergence difficulties due to quasi-ergodicity in the solid-liquid transition region. The heat capacity curves were found to differ markedly and nonmonotonically as functions of cluster size. Curves for  $N = 4, 5$  and  $8$  consisted of a smooth, featureless, monotonic increase throughout the transition region, while curves for  $N = 7$  and  $15$ – $17$  showed a distinct shoulder in this region; the remaining clusters had distinguishable transition heat capacity peaks. The size and location of these peaks exhibited “magic number” behavior, with the most pronounced peaks occurring for magic number sizes of  $N = 13, 19$  and  $23$ . This is consistent with the magic numbers found for many other cluster properties, but there are interesting differences for some of the other cluster sizes. Further insight into the transition region was obtained by comparing rms bond length fluctuation behavior with the heat capacity trends. A comparison of the heat capacities with other cluster

properties in the solid-liquid transition region that have been reported in the literature indicates partial support for the view that, for some clusters, the solid-liquid transition region is a coexistence region demarcated by relatively sharp, but separate, melting and freezing temperatures; some discrepancies, however, remain unresolved.

## I. INTRODUCTION

The investigation of small atomic and molecular clusters is an active area of current research, both theoretically<sup>1–16</sup> and experimentally.<sup>17–19</sup> Their small size (typically 3 to 150 atoms) makes clusters ideal candidates for computer simulation studies, and most theoretical studies to date have used Monte Carlo<sup>21–24</sup> and molecular dynamics methods.<sup>24–26</sup> Because of the large computational demands inherent in these simulation methods, most early theoretical investigations were limited to classical rare gas clusters bound by simple pairwise additive Lennard-Jones potentials, but continuing improvements in computer technology have led to an increasing number of more interesting metal cluster simulations requiring more sophisticated intermolecular potentials for physically realistic representation,<sup>27</sup> and have made quantum simulations based on Fourier path integral methods practical.<sup>28</sup>

One major motivation for the study of clusters is the insight that can be provided for understanding the transition from finite to bulk behavior. Many cluster properties show a very irregular dependence on the aggregate cluster size  $N$ . For example, the difference in the binding energy between successive pairs of rare gas clusters is especially marked for clusters of size  $N = 13, 19, 23, 26, 29, 39, 46, 49$ , and 55, and dramatically smaller for their immediate neighbors.<sup>29</sup> The mass spectrum intensity of Xe clusters formed by condensation in supersonic jets was found to increase slightly for sizes  $N = 13, 19, 25, 55, 71, 87$ , and 147 and then decrease sharply for the clusters immediately following in size.<sup>19</sup> Calculations of the Gibbs free energy of formation for argon clusters with sizes ranging from 2 to 20 indicated local minima for  $N = 7, 13$  and 19.<sup>20</sup> This nonuniform dependence of certain cluster properties on size, often termed “magic number” effects, has been of great theoretical interest. Much work has been done in relating magic number sequences to cluster structure in terms of “soft” sphere packings, since many magic number sizes such as  $N = 13, 19, 55$ , and 147 correspond to compact icosahedral based structures.<sup>29–31</sup>

An especially important phenomenon exhibiting magic number effects is cluster “melting.” Because of their small size, clusters do not have the sharp first order transition charac-

teristic of bulk melting, but instead show transitions occurring over a range of temperatures.<sup>4</sup> The transition range generally decreases as the cluster size increases, coalescing to the bulk transition temperature as  $N$  approaches infinity, but it shows a wide variety of behavior for smaller sizes. Berry and coworkers<sup>1</sup> have postulated that for certain sized clusters, the transition region is in fact a coexistence region where both “solid-like” and “liquid-like” isomers dynamically coexist, fluctuating back and forth between relatively long lived “solid” and “liquid” states. This implies that these clusters have sharp, but different, “freezing” and “melting” temperatures. Some of their molecular dynamics studies revealed that clusters with sizes  $N = 7, 9, 11, 13, 15$ , and  $19$  have especially high melting temperatures and pronounced coexistence ranges, while clusters with sizes  $N = 8, 14$  and  $20$  melt at much lower temperatures and exhibit no coexistence.<sup>4</sup>

The problem of cluster phase transitions, has been one of great interest, and one not lacking in controversy (Ref. 4 provides a good review). While many studies are consistent with the view of a dynamic coexistence between solid-like and liquid-like isomers in the transition region, other studies emphasize, instead, a relatively smooth progression of isomerizations between locally similar but globally distinct configurations occurring throughout the transition region.<sup>7</sup> In addition, it is becoming increasingly clear that the problem of incomplete sampling of configuration space for simulations run in the transition region is much more serious than had been appreciated earlier, and that extremely long simulations (much longer than those routinely used even a few years ago) are necessary to prevent large systematic errors in certain properties that can result in misleading interpretations. Given the large amount of contradictory evidence that has been accumulated over the years, as well as the problem of not knowing how reliable some of it is, it is apparent that the nature of cluster melting remains still very much unresolved.

There is no problem concerning cluster behavior at extreme temperatures. At very low temperatures, clusters are locked into solid structures having near rigid rotations and small amplitude, harmonic-like vibrations; there is no conversion between different isomers. At sufficiently high temperatures, the clusters dissociate, implying that for simulations run

under free volume conditions, the average energy vanishes in the limit of an infinite number of configurations.<sup>12–14</sup> Consequently, it is usual in Monte Carlo simulations to confine the cluster within a perfectly reflecting constraining potential having a typical radius of a few atomic radii that is centered on the cluster’s center of mass.<sup>16</sup> Under such conditions, the high temperature limit corresponds then to a highly compressed vapor confined to a small spherical cavity. This limiting behavior is evident in Fig. 1, which shows the average internal energy and heat capacity as functions of temperature for a typical small classical rare gas cluster. For  $T \rightarrow 0$ , the energy approaches the global minimum potential energy, and the heat capacity approaches the classical equipartition of energy result for a harmonically bound nonlinear system,  $3N - 3$ . For  $T \rightarrow \infty$ , the internal energy and heat capacity both approach their ideal gas limits.

What happens in between is less clear. In this case, the heat capacity curve has two distinct peaks, which would indicate two “phase” changes. Temperature driven first-order transitions in small systems are typically spread out over a finite range of temperatures, with the size of the transition region corresponding to the width of the heat capacity peak, and the transition temperature corresponding to the heat capacity maximum.<sup>4</sup> The larger, higher temperature heat capacity peak can be therefore associated with the transition from a condensed phase to the vapor phase (that is, cluster dissociation), while the smaller, lower temperature peak represents a solid-liquid transition. Not surprisingly, the size and location of the higher temperature peak have a sensitive dependence on the cluster simulation boundary conditions, and thus vary considerably as functions of the constraining radius. Their dependence on the cluster aggregate size is less pronounced, though, and quite regular. Hence the information conveyed in this region is somewhat artificial and lacking in physical importance. This is not the case for the solid-liquid transition, however. This peak is largely independent of the constraining radius, provided the radius is not so small that the free rearrangement of the cluster is limited. In addition, the solid-liquid transition region has a very marked dependence on cluster size; while all clusters confined in sufficiently large constraining spheres show a large dissociation peak in their heat capacity-temperature curve,

not all clusters show peaks in the solid-liquid transition region, and for those that do, the size and shape of the peak have a very nonuniform dependence on cluster size. Does the presence of a heat capacity peak in the solid-liquid transition region then necessarily imply a solid-liquid transition temperature corresponding to the peak temperature, and concomitantly, does the absence of a heat capacity peak there rule out a definite solid-liquid transition temperature? What is the connection between the transition region as defined by the heat capacity peak width and the coexistence region defined by the sharp, yet distinct, freezing and melting temperatures obtained from some molecular dynamics simulations? One would expect the two ranges to mostly coincide, but as will be seen, this is not always the case.

Despite the importance of heat capacities in characterizing cluster phase transitions, few cluster heat capacity studies have been reported in the literature, and most of these have been limited to special cases, particularly  $N = 13$ <sup>12,32–34</sup> and  $N = 55$ .<sup>34,35</sup> This is due to the notorious difficulty in extracting heat capacities with sufficient accuracy from simulations. A typical example of the poor convergence of heat capacities is given in Fig. 1. The heat capacity curve obtained from averages taken over  $10^5$  Monte Carlo passes (or  $23 \times 10^5$  moves) for each temperature point (a simulation length that was typical ten to fifteen years ago) is not even qualitatively correct, with the solid-liquid transition peak completely absent. The curve obtained from walk lengths of  $10^6$  passes (a length routinely achieved five years ago) does show a small solid-liquid transition peak, but one that is very much diminished. Even the curve based on  $10^7$  passes is quantitatively poor in this region. This poor convergence behavior is a result of the incomplete sampling of configuration space by the random walker, a phenomenon denoted as “quasi-ergodicity” by Valleau and Whittington.<sup>22</sup> Quasi-ergodicity arises in systems where the sample space contains two or more regions that have a very low transition probability, resulting in bottlenecks that effectively confine the sampling to only one of the regions.<sup>24</sup> In clusters such as  $\text{Ar}_{23}$ , the potential hypersurface consists of very deep wells, corresponding to stable solid isomers, separated by very large barriers. The resultant dichotomy of time scales characterizing the Monte Carlo random walks (or likewise, the molecular dynamics time evolution) produces rapid small-scale motion within

the wells, but very slow large-scale movement between them.<sup>36</sup> Because of the finite length of the walks (or trajectories), systematic errors result that diminish only with increasing length, disappearing in the limit of infinitely long walks (or trajectories). Interestingly, it is precisely these conditions that Berry and coworkers claim are necessary for the existence of a solid-liquid coexistence region in clusters;<sup>4</sup> it appears that the very nature of this region that makes it so physically intriguing also conspires to make its elucidation exceedingly difficult.

Recently, new methods have been developed that substantially reduce quasi-ergodicity and dramatically increase convergence in cluster Monte Carlo simulations in the transition regions, thus allowing even computationally difficult properties such as cluster heat capacities to be obtained to high accuracy. These methods are characterized by their emphasis on large scale motions, or jumps, of the random walker to other regions of configuration space and thus have been collectively termed “J-walking” (for jump-walking).<sup>37</sup> J-walking has been successfully applied to several systems, including binary metal clusters,<sup>38</sup> water clusters,<sup>39</sup> and clusters absorbed on surfaces.<sup>40</sup> Tsai and Jordan<sup>32,39</sup> have combined J-walking with histogram methods,<sup>41</sup> and recently, J-walking was extended to quantum systems.<sup>42</sup> With J-walking, it is now feasible to systematically study the dependence of the heat capacity on cluster size for a fairly large range of cluster sizes; the solid curves in Fig. 1 were obtained using J-walking.

I begin in Section II with a brief review of the J-walking method and a summary of the calculations undertaken. Section III describes the results obtained using J-walking for the heat capacities and potential energies as functions of temperature and cluster size for Lennard-Jones clusters ranging in size from 4 to 24 atoms. Also included are results obtained from similar standard Monte Carlo simulations, including rms bond length fluctuations, as well as comparisons with molecular dynamics simulations and other calculations reported in the literature for rare gas clusters in this range. Finally, in Section IV, I discuss my findings in the context of some of the controversies and ambiguities concerning cluster phase transitions that remain unresolved.

## II. METHOD

J-walking addresses the problem of quasi-ergodicity in standard Monte Carlo simulations based on the sampling algorithm proposed by Metropolis *et al.*,<sup>21</sup> hereinafter called Metropolis Monte Carlo, by coupling the usual small-scale Metropolis moves with occasional large-scale jumps that move the random walker to different regions of configuration space. For classical systems governed by a potential  $V(\mathbf{r})$ , the Metropolis method uses a random walk to sample configuration space, with each attempted move from the current location  $\mathbf{r}_i$  to a trial location  $\mathbf{r}_f$  determined by the acceptance probability,

$$P = \min\{1, q(\mathbf{r}_f|\mathbf{r}_i)\}, \quad (1)$$

where

$$q(\mathbf{r}_f|\mathbf{r}_i) = \frac{T(\mathbf{r}_i|\mathbf{r}_f)\rho(\mathbf{r}_f)}{T(\mathbf{r}_f|\mathbf{r}_i)\rho(\mathbf{r}_i)}, \quad (2)$$

is the acceptance ratio,  $\rho(\mathbf{r}) = Z^{-1} \exp\{-\beta V(\mathbf{r})\}$  is the Boltzmann distribution with  $Z$  the standard configuration integral and  $\beta = 1/k_B T$  the temperature parameter, and  $T(\mathbf{r}'|\mathbf{r})$  is the transition matrix or sampling distribution. The sampling distribution is usually generated from uniform deviates  $\xi$  over a finite stepsize range  $\Delta$  to give<sup>23</sup>

$$T(\mathbf{r}_f|\mathbf{r}_i) = \begin{cases} 1/\Delta & \text{for } |\mathbf{r}_f - \mathbf{r}_i| < \Delta/2, \\ 0 & \text{otherwise,} \end{cases} \quad (3)$$

and thus

$$q(\mathbf{r}_f|\mathbf{r}_i) = \exp\{-\beta[V(\mathbf{r}_f) - V(\mathbf{r}_i)]\}. \quad (4)$$

Attempted moves are generated according to  $\mathbf{r}_f = \mathbf{r}_i + (\xi - \frac{1}{2})\Delta$ , with the maximum stepsize  $\Delta/2$  usually adjusted to give acceptance probabilities of approximately 50%. The required size depends on the width of the Boltzmann distribution, and thus decreases with increasing  $\beta$ . This temperature dependence can lead to quasi-ergodic behavior whenever the stepsize becomes too small relative to the potential barrier heights and widths; the walker becomes



effectively trapped within a region of configuration space if too many small steps are required to surmount large, steep barriers within the duration of the walk. Thus, for a given walk length, there is a threshold temperature such that walks undertaken below that temperature are quasi-ergodic.<sup>37</sup>

The Boltzmann distribution's dependence on temperature that can lead to quasi-ergodicity can also be exploited to overcome it. Although the form of the Boltzmann distribution is largely dependent on the form of the underlying potential, with distribution maxima corresponding to potential minima, the widths of the distribution peaks have an inverse dependence on  $\beta$ , with higher temperatures resulting in wider distributions. In essence, higher temperature walkers are less constrained because their larger stepsizes allow them to overcome the potential barriers more effectively. Hence, a Boltzmann distribution generated at some higher temperature where the sampling is ergodic can be used by a lower temperature walker to make large-scale moves in configuration space. J-walking then occasionally replaces the usual attempted Metropolis moves with attempted jumps to positions occupied by such a higher temperature walker (J-walker). Because the peaks in the Boltzmann distribution correspond to the potential minima, the J-walker's motion remains biased about the minima, greatly increasing the likelihood an attempted jump would be accepted.

This scheme is equivalent to replacing the usual Metropolis transition matrix given by Eq. (3) with the Boltzmann distribution at the higher temperature whenever a jump is attempted,

$$T_J(\mathbf{r}_J|\mathbf{r}_i) = Z^{-1} \exp\{-\beta_J V(\mathbf{r}_J)\} \text{ for } 0 \leq \xi_J < P_J, \quad (5)$$

where  $P_J$  is the jump attempt probability,  $\beta_J$  is the J-walker temperature parameter, and  $\mathbf{r}_J$  is the J-walker's location. This gives an acceptance ratio of

$$q_J(\mathbf{r}_J|\mathbf{r}_i) = \exp\{(\beta_J - \beta)[V(\mathbf{r}_J) - V(\mathbf{r}_i)]\}. \quad (6)$$

The likelihood of an attempted jump being accepted depends on the two Boltzmann distributions' overlap, which is reflected by the value of  $q_J$ . In the high temperature limit  $\beta_J \rightarrow 0$ ,

the acceptance ratio reduces to the standard Metropolis expression given in Eq. (4). Because the Boltzmann distribution broadens as the temperature increases, J-walking in this limit reduces to indiscriminate jumping with a very large stepsize, and so the probability of a jump being accepted becomes very small. In the limit  $\beta_J \rightarrow \beta$ ,  $q_J(\mathbf{r}_J|\mathbf{r}_i) \rightarrow 1$  since the low temperature walker is now effectively sampling from its own distribution.

Two complementary implementations for generating the classical J-walker Boltzmann distributions were originally presented.<sup>37</sup> The two are another example of the commonly encountered trade-off between computer memory and speed. The first ran the J-walker in tandem with the low temperature walker, with the low temperature walker occasionally attempting jumps to the current J-walker position simply by using the current J-walker coordinates as its trial position. In the second implementation, the J-walker was run beforehand and the configurations generated during the walk stored periodically in an external array. Subsequent jump attempts were made by accessing the stored configurations via randomly generated indices. The tandem walker scheme has very little memory overhead, but has the disadvantage of requiring that the J-walker be moved an extra number of steps whenever a jump is attempted in order to reduce correlations between the two walkers that otherwise result in systematic errors. The number of extra steps needed depends on the temperature difference between the two walkers, increasing the computation time greatly as the difference becomes larger. This implementation then is more suited for parallel computers. On the other hand, the use of external distributions has only a modest computational overhead (mostly the time required to generate the distributions), but requires very large storage facilities for handling the distribution arrays. Because fast workstations having tens of Mb of RAM and Gb of disk storage are now affordable and quite common, while access to parallel computers is still much more limited, the implementation using externally stored distributions remains the method of choice and was the one used for all the J-walking calculations reported in this study.

J-walking simulations were run for all clusters in the range  $4 \leq N \leq 24$ . The clusters studied were modeled by the usual pairwise additive Lennard-Jones potential,

$$V = \sum_{i < j} V_{LJ}(r_{ij}),$$

$$V_{LJ}(r_{ij}) = 4\epsilon \left[ \left( \frac{\sigma}{r_{ij}} \right)^{12} - \left( \frac{\sigma}{r_{ij}} \right)^6 \right]. \quad (7)$$

Small clusters are known to become unstable beyond a threshold temperature that varies with the cluster size.<sup>12,14</sup> For the Lennard-Jones potential under free volume conditions, the average energy vanishes in the limit of infinitely long walks. Consequently, the choice of boundary conditions can greatly affect some cluster properties at higher temperatures.<sup>4</sup> I have followed Lee, Barker and Abraham<sup>16</sup> and have confined the clusters by a perfectly reflecting constraining potential of radius  $R_c$  centered on the cluster's center of mass. To maintain a common set of boundary conditions throughout the survey, the constraining radius was identical for all the clusters studied, with  $R_c = 4\sigma$ .

For physically realistic systems such as clusters, the Boltzmann distributions are too narrow for a single distribution to be used for J-walking over the entire temperature domain from the solid region to the dissociation region, and so the distributions had to be generated in stages. For each cluster, an initial J-walker distribution was generated from a long Metropolis walk at a temperature high enough for the sampling to be ergodic. This distribution was then used for J-walking runs to obtain averages of the potential energy and the heat capacity for a series of lower temperatures. The width of the J-walker distribution limited the effective temperature range for subsequent J-walking simulations. When the temperature difference between the distribution and the low temperature walker became too large, very few attempted jumps were accepted since the low J-walker configurations likely to be accepted were in the low energy tail of the distribution. At the temperature where the jump acceptance started becoming too small,<sup>43</sup> a new distribution was generated from the previous one, using J-walking to ensure it was ergodic as well. This distribution was then used to obtain data for the next lower temperature range, and then to generate the next lower temperature J-walker distribution, and so on, until the entire temperature domain was spanned. To ensure that the higher temperature J-walker distributions were free of any systematic errors large enough to adversely affect the sampling, the temperature

ranges were occasionally overlapped so that J-walking data collected near the end of one distribution's useful temperature range (as indicated by the low jump acceptance) could be compared with the data obtained from the beginning of the next distribution's useful temperature range (where the jump acceptance rate was high). For example, a J-walker distribution generated at  $T = 15$  K could be used to generate data over the temperature range  $11 \leq T \leq 15$  K. By generating the next distribution at  $T = 12$  K for use over the range  $8 \leq T \leq 12$  K, data for the overlapping range  $11 \leq T \leq 12$  K obtained from both distributions could be compared and checked for consistency. All the distributions checked in this manner were found to be consistent.

The classical internal energy and heat capacity were calculated by the usual expressions for an  $N$ -atom cluster (in reduced units),

$$\langle U^* \rangle = \frac{3NT^*}{2} + \langle V^* \rangle, \quad (8)$$

$$\langle C_V^* \rangle = \frac{3N}{2} + \frac{\langle (V^*)^2 \rangle - \langle V^* \rangle^2}{(T^*)^2}, \quad (9)$$

where  $U^* = U/\epsilon$ ,  $V^* = V/\epsilon$ ,  $C_V^* = C_V/k_B$ , and  $T^* = k_B T/\epsilon$ . In order to more easily compare the classical results with quantum simulations to be undertaken later, curves for  $\langle U^* \rangle$  and  $\langle C_V^* \rangle$  as functions of  $T^*$  were actually generated using Ne parameters, with  $\sigma = 2.749$  Å and  $\epsilon = 35.6$  K. The temperature mesh size was typically  $\Delta T = 0.02$  K, and was reduced to 0.01 K for the solid-liquid transition regions. Similarly, J-walker distributions were generated at Ne temperatures. All the J-walking simulations run for each temperature consisted of  $10^5$  warmup passes followed by  $10^7$  passes with data accumulation (100 walks of  $10^5$  passes each); the jump attempt frequency was  $P_J = 0.1$  throughout.

Table I lists the J-walker distribution particulars for clusters in the range  $4 \leq N \leq 12$ , while Table II lists them for the range  $13 \leq N \leq 24$ . For each cluster, the initial J-walker distributions were obtained at temperatures corresponding to the high temperature side of the cluster dissociation peak, where all the cluster configurations were completely fluid. In the original J-walking study for  $N = 13$ ,<sup>37</sup> the initial J-walker distribution was obtained at a temperature corresponding to the liquid region (just past the solid-liquid transition region)

where the sampling was thought to be ergodic, but in fact turned out not to be fully ergodic. When J-walking was extended to quantum systems and tested on  $N = 7$  clusters,<sup>42</sup> it was discovered that there was also much quasi-ergodicity in the region corresponding to the low temperature side of dissociation peak, and so it was necessary to begin the temperature scans at an even higher temperature. This region corresponds to a coexistence region where both liquid-like and partially dissociated configurations are in dynamic coexistence, and sampling difficulties can arise when single atoms leave the cluster and wander about nearby for several passes before recombining with the cluster. Effects of quasi-ergodicity in this region can be seen in the heat capacity curves for  $\text{Ar}_{23}$  in Fig. 1. On the high temperature side of the dissociation peak ( $T \gtrsim 80$  K) the J-walker curve coincides with the Metropolis curves for both  $10^6$  and  $10^7$  passes, while on the low temperature side of the peak ( $50 \text{ K} \lesssim T \lesssim 75 \text{ K}$ ) there are substantial discrepancies between the J-walking curve and the Metropolis curve obtained from  $10^6$  passes, and smaller discrepancies between the J-walking curve and the Metropolis curve obtained from  $10^7$  passes. Although these discrepancies are much smaller than those appearing in the solid-liquid transition region, it is important to minimize systematic errors in the J-walker distribution since the sensitivity of these errors on subsequent J-walking runs is not known.

All J-walker distributions consisted of  $10^6$  configurations, except for  $N = 4$  and  $N = 8$ , which had  $1.25 \times 10^6$  and  $0.75 \times 10^6$  configurations, respectively. The configuration energy and center of mass coordinates were also stored with the cluster coordinates so that they would not have to be recalculated during subsequent J-walker simulations whenever a jump was accepted. The required storage space for these distributions varied from 122 Mb (for  $N = 4$ ) to 580 Mb (for  $N = 24$ ), and so they were stored in 10 or 50 separate files, depending on the amount of computer primary memory that was available.<sup>44</sup> During a J-walking run, a file was randomly selected and read into memory. This array was used for sampling jump attempts for a while before being randomly replaced by another file. By making the files as large as possible within the memory constraints, disk access was reduced during the J-walking simulations, greatly improving their efficiency. Because the configurations generated during

Metropolis walks are highly correlated, they were stored in a periodic fashion. Initially, almost all distributions were generated by storing configurations every 100 passes, as can be seen in Table I for the smaller clusters. As the cluster size was increased, generating such distributions became very time consuming. Not only did it take longer to generate a distribution for a larger cluster, but more distributions were required to span the entire temperature range. Thus, for the larger clusters, only the widest distributions containing the greatest variety of configurations were sampled every 100 passes. Narrower distributions were sampled every 50 passes, and very narrow distributions for low temperatures corresponding to the solid region were sampled every 10 passes. Fig. 2 shows potential energy histograms for  $N = 11$  and  $N = 19$  clusters. The smaller cluster has a potential energy range about half that of the larger cluster, and so only five J-walker distributions were needed to span the entire temperature range from the solid region to dissociation, compared to the ten distributions required for the larger cluster. The spacing of the distributions requires some judgment. On the one hand, they should be spaced as far apart as possible to minimize the computational time needed to generate them. On the other hand, they should not be spaced so far apart that the number jumps accepted becomes too low and systematic errors arising from quasi-ergodicity corrupt the distributions. As can be seen in the plots, substantial overlap between adjacent distributions was required for reasonable jump acceptances (these are also listed in Tables I and II).

Correlations in the J-walker distributions were further reduced by writing the distribution files in a parallel fashion. All output distribution files were opened at the start of the program and configurations were written to each in turn, rather than writing to each file sequentially, one at a time. Thus, each distribution file contained configurations sampled from the entire run. Unfortunately, this resulted in highly fragmented files, which greatly increased the time required to later read a distribution into memory, since the files were all physically interleaved on the disk drive. This problem was easily solved, however, by simply copying the distribution files to a different directory, where they were written to the disk sequentially.

Since J-walking is still new, and experience with it is still being obtained, standard

Metropolis simulations were also run for each cluster. These provided a check of the J-walking results for those temperature regions where quasi-ergodicity in the Metropolis runs was not a problem, as well as revealing trends in the systematic errors arising from quasi-ergodicity in the Metropolis runs as functions of cluster size. Temperature scans were also generated using Ne parameters, with the temperature mesh size  $\Delta T = 0.02$  K. For each temperature, simulations consisted of  $10^5$  warmup passes, followed by  $10^7$  passes with data accumulation (again, 100 walks of  $10^5$  passes each). The scans were started at  $T = 0.2$  K from the global minimum configuration,<sup>29,30</sup> and continued past the cluster dissociation peak. The final configuration for each temperature was used as the initial configuration for the next temperature. For all of the clusters examined, the Metropolis and J-walking results agreed qualitatively throughout the entire temperature ranges, and agreed quantitatively throughout most of the temperature ranges, with discrepancies occurring mostly in the transition regions affecting the peak heights, especially for the larger sizes; the discrepancies seen in Fig. 1 for  $\text{Ar}_{23}$  were the largest obtained in this study.

One of the few cluster properties not amenable to calculation using J-walking is the relative rms bond length fluctuation,

$$\delta = \frac{2}{N(N-1)} \sum_{i < j} \frac{(\langle r_{ij}^2 \rangle - \langle r_{ij} \rangle^2)^{1/2}}{\langle r_{ij} \rangle}. \quad (10)$$

The averages are taken over an entire walk, and so are dependent on the walk length. With J-walking, a “walk” is really a collection of short excursions of a few steps duration beginning from the different points in configuration space that are accessed whenever a jump attempt is accepted, and so there is no continuous evolution of  $i$ - $j$  bonds over the entire length of the walk.

Rms bond length fluctuations have been calculated in many previous molecular dynamics and Metropolis Monte Carlo simulations and have been used as indicators of solid-liquid phase changes.<sup>1-3,13,33</sup> The fluctuations typically undergo a gradual, nearly linear increase as the temperature is increased in the solid region, then rise sharply in the transition region as the clusters begin to acquire enough energy to overcome the potential barriers to rearrange-

ment, and then level off somewhat in the liquid region. For magic number clusters such as  $N = 13$ , the rise can be very abrupt, while for other clusters, it is more gradual.<sup>3</sup> Like the heat capacity,  $\delta(T)$  is very difficult to calculate accurately in the transition region because of its sensitivity to quasi-ergodicity. This is evident in Fig. 3, which shows averages of  $\delta(T)$  for  $N = 13$  obtained from 10 Metropolis walks of  $10^4$ ,  $10^5$  and  $10^6$  passes in length; the lack of convergence in the transition region is clear. The systematic error throughout the transition region results in the  $\delta(T)$  curves for  $10^4$  and  $10^5$  passes occurring too high in the temperature region spanned by the heat capacity peak, whereas the curve for  $10^6$  passes rises sharply just as the heat capacity curve begins its rise. The curve for  $10^5$  passes is similar to the curve reported in Ref. 33, which was obtained from Metropolis walks of a similar length. This behavior can also be understood in terms of the potential energy hypersurface governing the random walks. For  $N = 13$ , the deep potential wells associated with various stable isomers are separated by large barriers. Temperatures near the point  $T_\delta^*$  where  $\delta(T)$  rises sharply correspond to energy distributions having a small fraction of energies in their tails that are on the threshold of overcoming the barriers to isomerization. Thus a walk length of  $10^6$  passes that resulted in even a few barrier crossings would be averaging the different fluctuations for different isomers, resulting in much larger values than those obtained from walks of  $10^5$  or  $10^4$  passes where the walker remained trapped in a single isomeric form for the duration of the walk.

This great sensitivity of the  $\delta(T)$  curve on the walk length brings into question then the appropriateness of applying to clusters the Lindemann criterion of liquid behavior occurring for  $\delta > 0.1$ , which has its basis from the study of bulk systems. For clusters, a value of  $\delta \approx 0.1$  obtained from sufficiently long walks actually corresponds to the threshold of isomerization where the cluster spends most of its time in some solid-like form with occasional isomerizations to another solid-like form, rather than to liquid behavior where the cluster atoms readily undergo diffusion. The region following the sharp rise where the curve levels off is more representative of liquid behavior in clusters. This point has been previously mentioned in accounting for the different energies observed in molecular dynamics simulations



between the onset of large bond length fluctuations and the onset of diffusion obtained from power spectra.<sup>3</sup>  $T_\delta^*$  is also much lower than the value obtained from molecular dynamics simulations reported in Ref. 3, although that value may also be too high considering the great sensitivity of  $\delta$  on the simulation length found in the Monte Carlo simulations. Care must be taken when comparing  $\delta$  values obtained from molecular dynamics simulations with those obtained from Monte Carlo simulations, though. Average rms bond length fluctuations can depend greatly on the ensemble used, and discrepancies between results obtained for  $\text{Ar}_{13}$  in the microcanonical ensemble with molecular dynamics and those obtained in the canonical ensemble with Monte Carlo have been noted previously.<sup>33</sup> Despite these problems,  $\delta(T)$  curves can still be very useful for providing insight into the solid-liquid transition region since their behavior also has a sensitive dependence on the cluster size.

Rms bond length fluctuations were not originally calculated with the Metropolis simulations described above, but in order to obtain more insight into some discrepancies in the transition region between the J-walking results and results obtained from molecular dynamics calculations reported in Ref. 3 that became apparent after the original Metropolis simulations had been run, temperature scans of  $\delta$  were subsequently obtained from additional Metropolis simulations. These were calculated at each temperature as averages taken over 10 walks, each having a length of  $10^6$  passes.

### III. RESULTS

Curves of the heat capacity per atom as functions of temperature for clusters ranging in size from  $N = 4$  to 12 and 13 to 24 are shown in Figs. 4 and 5, respectively. These were obtained from the J-walking studies. As is evident in these figures, the curves differ markedly and nonmonotonically with cluster size. There are three kinds of curves. For clusters of size  $N = 4, 5$  and 8, the heat capacity rises slowly from its classical equipartition value at  $T^* = 0$  until the temperature approaches the cluster dissociation region, where it then rises sharply. There is no peak in the solid-liquid region, although a very weak shoulder

is barely perceptible. Curves for clusters of size  $N = 7$ , and 15–17 also have no peak in the solid-liquid transition region, but they do show a distinct shoulder characterized by two inflection points, one at a lower temperature  $T_L^*$ , about halfway up the shoulder, and the other at a higher temperature  $T_H^*$ , at the top of the shoulder. All the other clusters studied have discernible heat capacity peaks in this region that can be characterized by an inflection point on the low temperature side of the peak (at  $T_L^*$ ), the peak maximum itself (at  $T_P^*$ ), and a local minimum on the high temperature side of the peak (at  $T_H^*$ ) between the peak and the dissociation region peak. These temperatures are indicated in Figs. 4 and 5 by the large ticks on the temperature axes; their values, together with their corresponding heat capacities, are also listed in Table III. The values for the peak and local minimum in each case were obtained by smoothing the J-walker data (note, however, the curves shown in Figs. 4 and 5 are the raw, unsmoothed J-walker data), interpolating the smoothed data to obtain a finer mesh size, and then searching for the maximum and minimum, respectively. The inflection points were obtained by using finite differences in the smoothed, interpolated data to generate derivatives, and then searching the resulting derivative curves for the maximum and minimum. Because there was some variation in the values obtained from various fits generated with different smoothing parameters, several fits were done for each cluster; the values reported are the averages obtained from the fits, and the uncertainty estimates are the standard deviations.<sup>45</sup>

For those clusters having peaks in the solid-liquid region, the transition temperature can be associated with the peak maximum, and the transition range with the peak width,<sup>4</sup> while for those clusters having shoulders in this region, the transition temperature can be estimated as the inflection point at the top of the shoulder. Although the transition temperature thus defined can be obtained easily for each curve, defining the transition range is more ambiguous. While the inflection points and local minima that characterize each peak may be unambiguous, their relation to the width of the transition region is less clear. In their original J-walker study of classical systems, Frantz, Freeman and Doll<sup>37</sup> observed that the onset of the transition region in  $\text{Ar}_{13}$  could be characterized by a sudden, sharp rise in the

heat capacity standard deviation obtained from Metropolis Monte Carlo simulations. For very low temperatures corresponding to the  $\text{Ar}_{13}$  solid region, the standard deviation was very low, and increased slowly with increasing temperature until about  $T^* = 0.20$ , where it quickly rose about tenfold, reaching a maximum at  $T^* = 0.25$ , and then decreased to a minimum at  $T^* = 0.34$  before rising again in the dissociation region. If the temperature of the sharp rise in the heat capacity standard deviation,  $T_\sigma^*$ , was taken to signify the beginning of the transition region, and the latter temperature was taken to signify the end of the transition region, then the resulting temperature range was found to coincide very well with the  $\text{Ar}_{13}$  transition region obtained from molecular dynamics calculations by Berry and coworkers.<sup>1</sup> Moreover, this behavior of the heat capacity standard deviations was consistent with their interpretation of the transition region being a coexistence region marked by sharp, but unequal, melting and freezing temperatures,  $T_m$  and  $T_f$ ; below  $T_f$ , only solid-like isomers exist, and above  $T_m$ , only liquid-like forms exist, but in between in the coexistence region, both forms dynamically coexist. Thus, the fluctuations in the heat capacity were very small for low temperatures since the clusters were locked into their minimum energy configurations, undergoing small, mostly harmonic oscillations. At the freezing temperature, the motion was highly anharmonic as the clusters began to have sufficient energy to overcome the large barriers in configuration space separating the deep wells associated with the different isomers. This hindered isomerization led to the sharp increase in the heat capacity fluctuations since the random walks were mostly confined to individual wells, but occasionally escaped to other wells. The fluctuations decreased again at the melting temperature because the energy was high enough for unhindered isomerization to take place; the random walker had free access to all of configuration space. To better see the connection between the solid-liquid transition region and the heat capacity fluctuations, I have also included in Figs. 4 and 5 standard deviation curves for the heat capacities obtained from the Metropolis Monte Carlo walks. These curves are too noisy to quantitatively define a solid-liquid transition range, but their general features provide insight into this region. The arrows in Figs. 4 and 5 indicate the temperatures  $T_\sigma^*$ . By taking  $T_\sigma^*$  to signify the beginning of the transition region and  $T_H^*$  to

mark the end, a definition of the transition range based solely on heat capacity behavior can be made,

$$\Delta T^* = T_H^* - T_\sigma^*. \quad (11)$$

The dependence on cluster size for  $T_\sigma^*$ , as well as for the heat capacity peak characteristic temperatures,  $T_L^*$ ,  $T_P^*$  and  $T_H^*$ , is illustrated in Fig. 6. Also shown is the dependence on size for their corresponding heat capacities. Because much of the behavior of cluster heat capacities is influenced by the structures of the lowest energy isomers, Fig. 6 also shows the size dependence on the differences in the minimum potential energy configurations between successive clusters, or the binding energy differences,<sup>29</sup>

$$\Delta E_b(N) = -\Delta V_{\min}(N) = -[V_{\min}(N) - V_{\min}(N-1)]. \quad (12)$$

The binding energy differences show magic number behavior for  $N = 7, 13, 19$  and  $23$ , as evidenced by these sizes being local maxima.

Berry and coworkers have also investigated many of the clusters included in this study. In one particular molecular dynamics study of coexistence behavior in rare gas clusters, they reported results for clusters of size  $N = 7, 8, 9, 11, 13, 14, 15, 17, 19, 20, 22, 26$  and  $33$ .<sup>3</sup> By checking for the onset and disappearance of a bimodal distribution in the short-time averaged kinetic energies, they found coexistence ranges for  $N = 7, 9, 11, 13, 15$  and  $19$ . They also reported temperatures  $T_{\delta,MD}^*$  corresponding to long-time averaged kinetic energy values at which the rms bond length fluctuations  $\delta$  rose sharply. For comparison, I have superimposed these values in Figs. 4 and 5, as well as the coexistence ranges  $\Delta T_c^* = T_m^* - T_f^*$  for those clusters where the authors found coexistence behavior. An interesting feature of the molecular dynamics rms bond length fluctuations for those clusters showing coexistence behavior is evident in Figs. 4 and 5. For the magic number sizes  $N = 7, 13$  and  $19$ ,  $T_\delta^*$  was near the middle of the coexistence range, nearly as high as the peak temperatures  $T_P^*$ , while for the other clusters showing coexistence behavior,  $N = 9, 11$ , and  $15$ , it was near the beginning of the range.

### A. Pre-icosahedral: $4 \leq N \leq 12$

The results of the three studies (the J-walking heat capacity curves, the Metropolis Monte Carlo heat capacity fluctuation curves, and the molecular dynamics coexistence ranges) are mostly consistent for the smaller clusters with sizes less than  $N = 13$ . For  $N = 4$  and 5, there is no abrupt change in either the heat capacity or the heat capacity fluctuations until the beginning of dissociation region, where both rise sharply.  $N = 6$  is the smallest cluster to show a peak (albeit a small one) in the heat capacity curve, and the heat capacity fluctuations show the sharp rise and slow decrease characteristic of a solid-liquid coexistence region.  $N = 7$  is the smallest cluster having pentagonal symmetry in its lowest energy isomer,<sup>30</sup> and is the smallest of the magic number sizes (although it is a rather “weak” magic number in comparison to  $N = 13, 19$  and  $23$ ), and so one might expect a more pronounced heat capacity peak than found for  $N = 6$ . However,  $N = 7$  has only a shoulder, although the heat capacity fluctuations are similar to those for  $N = 6$ , implying a similar solid-liquid coexistence region. Ref. 3 also reported a coexistence range for  $N = 7$ , and as can be seen in Fig. 4, this range coincides quite well with the heat capacity transition range defined by Eq. 11. The results for  $N = 8$  are very similar to those obtained for  $N = 4$  and 5, and are consistent with those reported in Ref. 3. Wales and Berry<sup>2</sup> argued that the striking difference in coexistence behavior between  $N = 7$  and  $N = 8$  can be explained in terms of the differences in their potential energy surfaces. For  $N = 7$ , the global minimum corresponds to a very compact, stable structure, the pentagonal bipyramid, which lies much lower in energy than the other low-lying isomers and is separated from them by large barriers, preventing any easy isomerization. For  $N = 8$ , however, the global minimum corresponds to a pentagonal bipyramid with the eighth atom located on one of its ten equivalent faces. Degenerate isomers corresponding to moving the eighth atom to another face are separated by low barriers, as is a second isomer, which lies only slightly higher in energy. Thus  $N = 8$  clusters have easy access to the various potential wells and exhibit facile rearrangements. Heat capacity fluctuations remain small until the dissociation region since the random walker

experiences no bottlenecks in configuration space. Likewise for  $N = 4$  and 5. Although their minimum energy configurations (tetrahedron and trigonal bipyramid, respectively) are compact and stable, their barriers to interconversion to other isomers are small.

The heat capacity results obtained for  $N = 8$  appear to be contrary to some of the results obtained by Adams and Stratt,<sup>7</sup> who performed an instantaneous normal mode analysis on  $\text{Ar}_7$ ,  $\text{Ar}_8$  and  $\text{Ar}_{13}$ . They observed transition regions for both  $\text{Ar}_7$  and  $\text{Ar}_8$  based on the temperature dependence of the average percentage of imaginary frequencies, but found no evidence of a coexistence region in either. They also reported other dynamical similarities between the two clusters, and interpreted their results to imply that the solid-liquid transition should not be viewed primarily in terms of jumps between rigid and fluid structures, but as being a smooth progression through an ever increasing number of structural isomers that are locally similar, but globally distinct. The striking difference between the heat capacity curves for  $N = 7$  and 8, as well as between their heat capacity fluctuations, seems to indicate an inherently different transition behavior for these two clusters, and the consistency between these results and the molecular dynamics results lends further support to the coexistence view. However, not all the properties show such a large degree of dissimilarity. Self diffusion constants calculated by Adams and Stratt for  $\text{Ar}_7$  and  $\text{Ar}_8$  as functions of temperature were very similar,<sup>46</sup> and curves of the rms bond length fluctuations  $\delta$  as functions of temperature for these two clusters are more alike than different. Although the featureless nature of the  $N = 8$  heat capacity curve might imply that this cluster does not have a solid-liquid transition region, the diffusion constant behavior and the rms bond length fluctuation behavior suggest otherwise. The  $\delta(T)$  behavior can be seen in Fig. 7, which shows curves for  $N = 4$ –6 and 7–9. Both the  $N = 7$  and 8 curves show the sharp rise in  $\delta(T)$  that is characteristic of a transition. Although the heat capacity curves for  $N = 4$ , 5 and 8 are very similar in their lack of significant features in the solid-liquid transition region, only the  $N = 4$   $\delta(T)$  curve has a likewise featureless rise through the transition region, implying that no solid-liquid transition occurs before the cluster dissociates. Surprisingly then, the absence of a peak or shoulder in the heat capacity curve does not necessarily correspond to

the absence of a transition. One important difference for the  $N = 7$   $\delta(T)$  curve is that its sharp rise occurs at a significantly higher temperature than that of its immediate neighbors (it is almost as high as that for  $N = 9$ ). This was also the case for the molecular dynamics results reported in Refs. 2 and 3. As will be seen, this is a common feature of the other magic number clusters, and is another manifestation of their inherent stability.

The heat capacity curves for  $N = 9$  to 12 all exhibit small heat capacity peaks in the solid-liquid transition region, and their Metropolis Monte Carlo heat capacity fluctuations show the sharp rise and slow decrease characteristic of coexistence behavior. Ref. 3 reported results for  $N = 9$  and 11, and coexistence regions were found for both clusters. Again, the coexistence ranges obtained from the molecular dynamics calculations coincide very well with the transition ranges obtained from the heat capacities. The lowest energy isomers for these clusters represent the building up from  $N = 7$  by the successive addition of atoms to the five faces of the pentagonal bipyramid core, with the  $N = 12$  structure then being one atom short of an icosahedron. This regular progression is reflected in the heat capacity curves. The  $N = 9$  peak is small and close enough to the dissociation peak that it is barely more than a shoulder. The  $N = 10$  and  $N = 11$  peaks are slightly larger, and remarkably alike. The  $N = 12$  peak is considerably larger than the others. The transition ranges also show quite a regular progression, as is evident in Fig. 6, with the  $N = 9$  range being the smallest and occurring at the lowest temperature. The  $N = 10$ , 11 and 12 transition ranges are about equal in size, but occur at increasingly higher temperatures.

### **B. Icosahedral to Double Icosahedral: $13 \leq N \leq 19$**

The results for the range  $N = 13$  to 19 are consistent with the molecular dynamics results for the magic number endpoints  $N = 13$  and 19, but there are some surprising differences for sizes in between.  $N = 13$  is the prototypical magic number cluster and has been the subject of many investigations. Its minimum energy configuration is the icosahedron, a compact structure that is extremely stable. The  $N = 13$  potential energy surface is characterized

by very deep wells, corresponding to the icosahedral isomers, which are separated by large barriers and lie far below the wells corresponding to the next lowest energy isomers. Its heat capacity behavior is a reflection of the shape of this potential energy surface. The curve has a very large, pronounced peak in the solid-liquid region (more than double the height of the preceding  $N = 12$  peak), and the fluctuations in the heat capacities obtained from Metropolis Monte Carlo simulations show the characteristic features of a coexistence region. The coexistence range obtained from molecular dynamics calculations reported in Ref. 3 also coincides very well with the transition region found in this study.

The J-walking results also agree with the original J-walking results for  $\text{Ar}_{13}$  reported in Ref. 37, except for a small discrepancy in the peak height where a value of  $\langle C_V^* \rangle / N = 9.37 \pm 0.04$  was obtained at  $T_P^* = 0.285 \pm 0.004$ , compared with  $\langle C_V^* \rangle / N = 9.06 \pm 0.01$  obtained at  $T_P^* = 0.2875 \pm 0.0007$  in this study. This investigation was more thorough than the original one. In that study, computer constraints limited the J-walker distribution sizes to only  $5 \times 10^4$  configurations, and walk lengths for each temperature consisted of  $10^7$  moves. In this study, J-walker distributions were twenty times larger, and walks consisted of  $10^7$  passes, and so were thirteen times longer. In addition, the first J-walker distribution in the original investigation was obtained from a long Metropolis Monte Carlo walk at  $T^* = 0.42$ . This was a temperature thought to be in the liquid region (and thus presumed to be free of quasi-ergodicity), but was actually near the beginning of the dissociation region where quasi-ergodicity again begins to become problematic. Since subsequent lower temperature J-walker distributions were generated in sequence from this distribution, any systematic errors in the distribution could have propagated to the other distributions and thus affected the J-walking results. In this study, the initial J-walker distribution was generated at  $T^* = 0.618$ , a temperature on the high temperature side of the dissociation region heat capacity peak where the heat capacity fluctuations had dropped substantially, thus reducing systematic errors in the lower temperature distributions. Despite these problems, the earlier J-walking study still gave a value for the heat capacity peak that was within 4% of the value obtained in this study for not much more computational overhead than the similar Metropolis Monte



Carlo simulation also reported in Ref. 37, which had an error of 19% for the peak height.

Further support for the accuracy of the results reported here can be found in a recent study by Tsai and Jordan,<sup>32</sup> who combined histogram and J-walking methods to calculate heat capacity curves for  $\text{Ar}_{13}$ . They obtained a peak height of  $\langle C_V^* \rangle / N = 9.01$  at  $T_P^* = 0.286$ , which is very close to the value reported here; the size of the difference between my values and theirs is similar to the small variations they observed for results obtained using different constraining sphere radii (their results were obtained using a smaller constraining radius, with  $R_c = 10 \text{ \AA}$ , or  $2.94\sigma$ , compared to  $R_c = 4\sigma$  used in this study). Finally, the results obtained from the Metropolis runs of the same length ( $10^7$  passes) agree with the J-walker results, with  $\langle C_V^* \rangle / N = 8.97 \pm 0.04$  and  $T_P^* = 0.2865 \pm 0.0011$ . This indicates that Metropolis walk lengths of  $10^7$  passes are sufficiently long to overcome quasi-ergodicity for  $N = 13$ , consistent with the findings of Tsai and Jordan, who reported that walk lengths of  $6 \times 10^6$  passes were sufficiently long.

The results obtained for  $N = 14$  to  $18$  are surprising, and are considerably different from the results obtained for  $N = 8$  to  $12$ . This was unexpected since the two ranges are analogous in many respects. Both are bounded by magic number sizes ( $N = 7$  and  $13$ , and  $N = 13$  and  $19$ , respectively) and have a similar “growth” sequence in their minimum energy configurations. This can be seen in Fig. 8, which shows the minimum energy configurations for  $N = 8$  to  $19$ .<sup>47</sup> Where the  $N = 8$  lowest energy isomer consists of a lone atom located on one of the ten faces of the  $N = 7$  pentagonal bipyramid core, and where the succeeding lowest energy isomers can be formally obtained by the addition of atoms in a fivefold symmetric manner, with the sixth capping the ring to form the  $N = 13$  icosahedron, the  $N = 14$  lowest energy isomer likewise consists of a lone atom located on one of the twenty equivalent icosahedral faces, and the succeeding lowest energy isomers (except  $N = 17$ ) can be likewise formally obtained by the addition of atoms in a fivefold symmetric manner, with the sixth capping the ring to form the  $N = 19$  double icosahedron (the expected  $N = 17$  configuration obtained in this manner is only slightly higher in energy than the actual minimum energy isomer shown, with an energy  $V^* = -61.3071$ , compared to  $V_{\min}^* = -61.3180$ ). The striking

similarity in the binding energy differences for these two ranges can be seen in the plot of  $\Delta E_b(N)$  shown in Fig. 6 — the sequence for  $N = 8$  to 13 is nearly identical to the sequence for  $N = 14$  to 19. Molecular dynamics calculations reported in Ref. 3 also found analogous behavior. Both  $\text{Ar}_7$  and  $\text{Ar}_{13}$  had relatively large coexistence ranges, while neither  $\text{Ar}_8$  nor  $\text{Ar}_{14}$  showed any coexistence behavior, and both  $\text{Ar}_9$  and  $\text{Ar}_{15}$  showed coexistence behavior, but had narrower ranges than  $\text{Ar}_7$  and  $\text{Ar}_{13}$ . Wales and Berry<sup>2</sup> ran extensive molecular dynamics simulations combined with quench studies for  $\text{Ar}_7$ ,  $\text{Ar}_8$ ,  $\text{Ar}_{13}$  and  $\text{Ar}_{14}$  that confirmed the earlier results. Yet, the heat capacity curves obtained with J-walking depicted in Figs. 4 and 5 are not at all consistent with these results. Where the  $N = 8$  heat capacity curve is featureless in the solid-transition region, the  $N = 14$  curve shows a clear peak. The peak is much diminished relative to the  $N = 13$  peak, but is nonetheless quite substantial; it is larger than the  $N = 12$  peak, which is the largest peak for  $N < 13$ . The fluctuations in the Metropolis heat capacities are consistent with the J-walking results, showing only a moderately steep rise followed by a slow decrease, suggesting some coexistence behavior. The results for  $N = 15$  are even more surprising in comparison. Ref. 3 reported a coexistence region for  $\text{Ar}_{15}$ , analogous to  $\text{Ar}_9$ , but the J-walking results reveal only a shoulder in the heat capacity curve over this region. While this does not rule out a coexistence region (as evidenced by the shoulder in the heat capacity curve for  $N = 7$ , which does show coexistence behavior), it does, then, make the absence of the coexistence region in the  $N = 14$  molecular dynamics simulations look even more puzzling by comparison. The behavior of the Metropolis heat capacity fluctuations for  $N = 15$  is also very different; the typical sharp rise signifying the onset of the coexistence region has been replaced by a more gradual increase that rises slowly over the domain spanned by the shoulder before beginning the usual rise in the dissociation region. The inflection points characterizing the heat capacity curve occur well after the molecular dynamics coexistence region, and the rise in the fluctuations occurs well before, resulting then in a very much larger transition region.

Rms bond length fluctuation curves for  $N = 13$ , 14 and 15 are shown in Fig. 9. As with  $N = 7$ , magic number behavior is manifested in  $N = 13$  by its much higher temperature  $T_\delta^*$

signifying the sharp rise in  $\delta(T)$ . Further similarities between  $N = 14$  and  $N = 15$  are evident in the  $\delta(T)$  curves. Except for the unusual smaller rise in  $\delta(T)$  beginning at  $T^* = 0.064$  for  $N = 14$ , the two curves differ very little. This smaller rise is likely due to the facile movement of the extra atom for  $N = 14$  on the icosahedral core. The average potential energy corresponding to this temperature is  $V^* = -46.60$ , which is comparable to the saddle point energy of  $-47.06$  representing the edge-bridging isomerization that moves the fourteenth atom from one icosahedral face to a neighboring one. It is also comparable with two other saddle point energies of  $-45.95$  and  $-45.84$ , which also represent isomerizations to degenerate capped icosahedrons.<sup>2</sup>

$N = 16$  continues the trend from  $N = 15$ , with the heat capacity curve reduced to an even smaller shoulder, and with the Metropolis heat capacity fluctuations remarkably uniform throughout the solid-liquid region. The results for  $N = 17, 18$  and  $19$  mirror the results for  $N = 13, 14$  and  $15$ , with  $N = 17$  having a shoulder in its heat capacity curve similar to the  $N = 15$  curve,  $N = 18$  having a moderate peak similar to the  $N = 14$  peak, and  $N = 19$  having pronounced peaks in both the heat capacity and the Metropolis heat capacity fluctuation curves, consistent with its magic number status. The only significant difference is that the shoulder and peak sizes for  $N = 17, 18$  and  $19$  are smaller than their counterparts for  $N = 15, 14$  and  $13$ . Interestingly, the rms bond length fluctuation curve for  $N = 18$  also mirrors the  $N = 14$  curve with a smaller rise beginning at  $T^* = 0.106$  and ending at  $T^* = 0.168$ , where it rises sharply. Further evidence of magic number behavior in  $N = 19$  is evident in the  $\delta(T)$  curves shown in Fig. 9, where once again  $T_\delta^*$  can be seen to occur at a much higher temperature than that of the next two larger clusters. The molecular dynamics coexistence range for  $N = 19$  reported in Ref. 3 also coincides quite well with the transition range I obtained, although it is slightly contracted.

### C. Beyond Double Icosahedral: $20 \leq N \leq 24$

The results for  $N = 20$  to  $24$  also differ substantially from those of  $N = 14$  to  $18$ . This is not unexpected since the minimum energy configurations for these clusters show a considerably different structural sequence, with additional atoms occupying sites between the three equatorial 5-atom rings of the  $N = 19$  double icosahedron. Fig. 10 shows the minimum energy configurations for  $N = 20$  to  $24$ . For  $N = 23$ , the additional atom caps an interpenetrating icosahedral substructure, resulting in a magic number configuration. Magic number behavior can be seen in Figs. 5 and 6 by both the large heat capacity peak and in the binding energy difference maximum. The heat capacity peak is about the same size as the previous magic number cluster,  $N = 19$ . The Metropolis heat capacity fluctuations also show the sharp rise and larger peak indicative of a coexistence region.

Unlike  $N = 14$ , whose heat capacity peak is much smaller than its preceding magic number  $N = 13$  peak, the peaks for  $N = 20$  and  $24$  are only slightly smaller than their preceding magic number peaks. The major differences between  $N = 19$  and  $20$ , as well as between  $N = 23$  and  $24$ , lie at the beginning of the transition regions. While the heat capacity fluctuations for  $N = 19$  and  $N = 23$  show the sharp rise and subsequent slow decline characteristic of a coexistence region, the fluctuations for  $N = 20$  and  $N = 24$  show a more gradual rise to a smaller maximum, followed by a slow decline. This was also the case for  $N = 21$  and  $22$ , and so determining the onset of the transition region for each of these clusters was ambiguous. As with  $N = 14$ , there was no evidence from molecular dynamics calculations of a coexistence region reported for  $N = 20$  in Ref. 3, which is surprising since its heat capacity peak is nearly as large as that for  $N = 19$  and its heat capacity fluctuations are also quite pronounced. The heat capacity curves and Metropolis heat capacity fluctuations are remarkably alike for  $N = 21$  and  $22$ , reminiscent of the similarity between  $N = 10$  and  $11$ . Both  $N = 21$  and  $22$  also have smaller peaks than the other clusters in this range. Molecular dynamics results for  $N = 22$  were also reported in Ref. 3 and no evidence of a coexistence region was found.

## IV. DISCUSSION

Although the heat capacity-temperature curves do not provide the definitive measure of the cluster solid-liquid transition region, they do serve as yet another useful probe into this region, providing additional data of surprising diversity and complexity that needs to be examined in terms of the various theories that have been proposed. Many of the results reported here are consistent with the view that for some clusters (especially for the magic number sizes), the solid-liquid transition region corresponds to a coexistence region with sharply defined, but separate, melting and freezing temperatures. Just how sharp these transition temperatures really are remains an open question, but for some clusters, properties obtained from Metropolis simulations such as the heat capacity fluctuations and rms bond length fluctuations do exhibit threshold-temperature behavior, with abrupt changes occurring over narrow temperature ranges. For many of the clusters where molecular dynamics simulations found evidence of coexistence behavior, the Metropolis heat capacity fluctuations were consistent, and the transition ranges obtained from Metropolis heat capacities coincide quite well with the coexistence ranges. But there are also some puzzling discrepancies, such as with  $N = 14$  and  $15$ . Molecular dynamics simulations found evidence of coexistence behavior for  $N = 15$ , which has neither a heat capacity peak nor an appreciable change in the heat capacity fluctuations throughout the solid-liquid transition region, but found no coexistence behavior for  $N = 14$ , which does have a heat capacity peak and an increase in the fluctuations. On the other hand, the view of the solid-liquid transition being a series of isomerizations through an ever increasing number of structures also appears consistent with my findings for some of the clusters studied, but it seems hard pressed to account for the entire range of behavior seen in the heat capacity curves and rms fluctuations. In addition, some supporting evidence is contrary to the heat capacity behavior. For example, the instantaneous normal mode analysis of  $N = 7$  and  $8$  indicated similar behavior in the transition region, but the heat capacity studies showed them behaving very differently. Similarly, the instantaneous normal mode analysis of  $N = 13$  indicated

no abrupt changes for some dynamical properties in the transition region, where the heat capacity, its fluctuations, and the rms bond length fluctuations all show abrupt changes.

It is also clear (for these smaller clusters, at least) that heat capacity peaks by themselves are incomplete measures of the solid-liquid transition region. For example, both  $N = 19$  and  $N = 20$  have similarly sized heat capacity peaks, but  $N = 19$  also shows magic number behavior in its binding energy and rms bond length fluctuations, and shows coexistence behavior according to molecular dynamics simulations, while  $N = 20$  exhibits none of these. Even the absence of a heat capacity peak in the solid-liquid region is no indication of the absence of a transition there. The curves for  $N = 4, 5$  and  $8$  are all featureless in this region, but rms bond length fluctuation curves for  $N = 5$  and  $8$  show evidence of a solid-liquid transition.  $N = 7$  is a magic number cluster, but its heat capacity curve has no peak, even though its non-magic number predecessor  $N = 6$  does have a heat capacity peak.

Additional insight into the solid-liquid transition region can be obtained by comparing the heat capacity magic number behavior with that of other properties. Fig. 6 shows that the heat capacity magic numbers are the same as the  $\Delta E_b(N)$  magic numbers over the range  $4 \leq N \leq 24$ , but there are interesting differences between the two sequences. The magic numbers for the  $\Delta E_b(N)$  sequence are  $N = 7, 13, 19$  and  $23$ , as evidenced by these sizes having the largest values (except for  $N = 7$ , which has the largest value for  $N < 9$ ). In each case,  $\Delta E_b(N)$  substantially decreases for  $N$  immediately following, and then rises. The magic numbers for the heat capacity are likewise  $N = 7, 13, 19$  and  $23$ , which are the local maxima in the heat capacity peak sequence. However, with the exception of  $N = 8$ , which has a featureless transition region, the peaks for  $N = 14, 20$  and  $24$  do not show a corresponding dramatic decline followed by an increase. Instead, there is a gradual decline over several sizes.  $N = 14$ , which has a small peak, is followed by three clusters having smaller shoulders, while  $N = 20$  has nearly as large a peak as the  $N = 19$  peak, and  $N = 24$  has a peak only slightly smaller than the  $N = 23$  peak. Furthermore, the heat capacity peak sequence for  $N = 8$  to  $13$  does not show the remarkable similarity with the  $N = 14$  to  $19$  sequence that is evident in the  $\Delta E_b(N)$  values. Thus, it appears a cluster's minimum

energy structure has a dominant influence on the heat capacity only for the magic number sizes.

The impact of the minimum energy structure on cluster energetics for magic number sizes is also evident in Fig. 11, which plots for all the clusters studied the potential energies per atom as functions of temperature. The curves have a roughly uniform spacing for temperatures corresponding to the liquid region, while for temperatures in the solid region, the curves show the nonuniform spacing expected for the very different geometrical structures associated with each minimum energy configuration, with the enhanced stability of the magic number clusters  $N = 13, 19$  and  $23$  (and to a lesser extent,  $N = 7$ ) clearly evident. Also included in the plot are the  $T_\sigma^*$  values and the heat capacity peak temperatures,  $T_L^*$ ,  $T_P^*$  and  $T_H^*$ , which characterize the transition region. The nonuniform spacing of the solid region and the enhanced stability of the magic number structures persist through much of the transition region, as does the uniform spacing of the liquid region. This indicates that both solid-like and liquid-like forms are indeed found in the region spanned by the heat capacity peak. The persistence of solid-like forms into the transition region and the enhanced structural stability of the magic number sizes can be seen even more dramatically in Fig. 12, where the  $\Delta E_b(N) = -\Delta V^*(N)$  curve for zero temperature shown in Fig. 6 has been generalized to nonzero temperatures to form the surface  $-\Delta\langle V^*(N, T) \rangle = -[\langle V^*(N, T) \rangle - \langle V^*(N-1, T) \rangle]$ , with the temperature range spanning the solid-liquid transition region up to the beginning of the dissociation region of the larger clusters. The icosahedral based magic number sizes  $N = 13, 19$  and  $23$  are especially noticeable — the  $-\Delta\langle V^* \rangle$  peak values differ very little from their zero temperature values well into the transition region, until their abatement over a relatively narrow temperature range at the heat capacity peak temperature. This temperature range is much smaller than the transition range defined in Eq. 11, beginning at about  $T_L^*$  rather than at  $T_\sigma^*$  and ending well before  $T_H^*$ . Although this seems to indicate more the abrupt change from solid to liquid rather than the coexistence of solid and liquid forms over an extended range, it must be remembered that these energy differences are between average energies, which can be quite insensitive to the makeup of their underlying

distributions.

The average potential energy and configurational heat capacity at a given temperature are of course just the first two moments of the potential energy distribution for that temperature, and so they represent only a minimal description of the distribution. Further insight into cluster energetics can be obtained by examining the distributions themselves. With J-walking, accurate potential energy distributions can be obtained during a simulation at a given temperature by binning the potential energies during the walk and forming a histogram. For example, the distributions shown in Fig. 2 were obtained this way. By projecting several histograms over a temperature range, a distribution surface can be formed as a function of the potential energy and temperature. Fig. 13 shows examples of such surfaces. These are for the range  $N = 13$  to 18, which contains representative samples of the different types of heat capacity behavior encountered (a strong peak at  $N = 13$  declining to a weak shoulder at  $N = 16$  and then rising again to a strong peak at  $N = 19$ ). Narrow distributions occur at the temperature extremes corresponding to the solid and dissociation regions; saddle points correspond to the widest distributions and thus represent heat capacity peaks. Not surprisingly, the change in the distributions in the solid-liquid transition region is much more abrupt for  $N = 13$  than for the other clusters. Not only do the distributions for the solid region widen appreciably and then narrow suddenly for the liquid region to form the characteristic hump on the surface, but the distributions for the two regions are partially offset, indicating a bimodal distribution. This is evident in Fig. 14, which shows the potential energy distributions for temperatures near the heat capacity peak temperature  $T_P^*$ . The bimodal distribution indicates well separated energies that can be associated with distinct solid-like and liquid-like forms and thus are further evidence of coexistence behavior in  $N = 13$ . Unfortunately,  $N = 13$  is the only cluster in the range studied that clearly has a bimodal distribution in the solid-liquid transition region. As can be seen in Fig. 14, even the other magic number clusters  $N = 19$  and  $N = 23$ , which have similar distribution surfaces with a similar widening at the heat capacity peak temperature, do not show clear bimodality there. This does not rule out coexistence behavior, though, since the two distributions



might overlap enough to show only a single maximum, but it does indicate that the different distributions are not widely spaced apart, like they are in  $N = 13$ .

The distribution surfaces for  $N = 15, 16$  and  $17$  show a very smooth, gradual evolution from the sharp, narrow distributions in the solid region to the broader distributions in the liquid region. This behavior is consistent with the view of the solid-liquid transition being a progression through an increasingly large number of structural isomers. For these clusters then, there are no threshold changes in the potential energies being accessed as the temperature increases past the solid region — higher energy isomers with energies slightly higher than the minimum energy isomer are separated by low barriers and thus are easily accessible.  $N = 16$  clusters have several local minima lying close to the global minimum,<sup>11</sup> as does  $N = 17$ ,<sup>1</sup> which also has a local minimum differing by less than 0.02%. The similarity between these three clusters is also evident in the behavior of their average potential energy per atom. As can be seen in Fig. 11, the spacings between the curves for these clusters are almost equal and change very little throughout the temperature range. Again, this is very much different than the behavior displayed by the magic number clusters.

Further evidence of the coexistence between solid-like and liquid-like isomers for the magic number clusters in the transition region comes from the rms bond length fluctuation curves. Comparison of the  $\delta(T)$  curves shown in Fig. 9 with the  $-\Delta\langle V^*(N, T) \rangle$  surface in Fig. 12 reveals that the temperatures  $T_\delta^*$  where the fluctuations for each cluster rise sharply from their nearly linear increase in the solid region (thus marking the onset of hindered isomerization) are well below the temperatures where the  $-\Delta\langle V^*(N, T) \rangle$  peaks diminish quickly, implying that the solid-like forms persist well into the transition region (although undergoing increasingly frequent isomerizations). However, the end of the sharp rise and the leveling of the  $\delta(T)$  curves to a value of about 0.3 also occurs in this region, indicating liquid-like behavior there as well. Note also that the lack of change in the average potential energy difference between  $N = 14$  and  $N = 13$  up to a reduced temperature of about 0.25 lends further support to the conjecture that the initial rise in  $\delta(T)$  for  $N = 14$  is due to the motion of the lone atom on the icosahedral core, rather than an isomerization to one of the

other low-lying configurations.

Magic number behavior in  $T_\delta^*$  is shown in Fig. 15, which plots the  $T_\delta^*$  values obtained from the Metropolis simulations against cluster size. Magic number behavior is evident for  $N = 13, 19$  and  $23$  (and to a lesser extent for  $N = 7$ ) by their much higher  $T_\delta^*$  values. The  $T_\delta^*$  values for all the clusters lie below  $T^* = 0.18$ , which according to Figs. 11 and 12 places them near the end of the solid region. Also, as can be seen in Fig. 15, they generally coincide with the  $T_\sigma^*$  values obtained from the rise in the heat capacity fluctuations, further supporting the claim that this region marks the beginning of the transition. Given the large degree of ambiguity in determining either  $T_\sigma^*$  or  $T_\delta^*$  for some of the larger clusters because of the large levels of noise in their fluctuations, it is not valid to conclude much more than the general observation that these values increase slightly with increasing cluster size, except for magic number sizes, where they occur at much higher temperatures.

Also included in Fig. 15 are the  $T_{\delta,MD}^*$  values obtained from molecular dynamics simulations reported in Ref. 3. Although these values are all significantly higher than the Metropolis values, their pattern is quite similar, with the magic number clusters having values that are substantially higher than those of their immediate neighbors. As noted earlier, the discrepancies between the two sets of data result from the shorter trajectory lengths used in the molecular dynamics simulations, and from the different ensembles associated with each method.<sup>33</sup>

Those clusters exhibiting coexistence behavior also have their coexistence ranges shown in Fig. 15. Except for  $N = 15$ , which has a coexistence range, contrary to the heat capacity behavior, and  $N = 20$ , which has no coexistence range even though the heat capacity data suggests it should, the correspondence between the coexistence ranges and the transition ranges defined by the heat capacity behavior is quite good. For  $N = 7, 9, 11, 13$  and  $19$ , both studies give consistent evidence of coexistence behavior, and the size and location of the two ranges are similar, while for  $N = 8, 17$  and  $22$ , the lack of evidence of coexistence behavior is likewise consistent. Unlike most of the molecular dynamics results used as evidence for the coexistence region, though, the heat capacity results obtained from the

Monte Carlo simulations are equilibrium properties and thus provide mostly inferential, not direct, evidence of dynamical coexistence between solid-like and liquid-like forms. The large degree of consistency between the two does lend strong support to the hypothesis, but the discrepancies for  $N = 15$  and  $N = 20$  are troubling in that they have no obvious resolution. While it appears that quasi-ergodicity is an even more insidious problem than has been appreciated in the past, one cannot simply dismiss these discrepancies as being due to improper sampling in the molecular dynamics simulations without accounting for the good agreement for the other sizes, which were simulated in similar manner (also, it is the magic number sizes that are most prone to quasi-ergodicity problems, and these are the sizes where agreement is the strongest). The discrepancies might be the result of the different ensembles used,<sup>48</sup> since some cluster properties have a strong ensemble dependence. However, comparison of ensemble sensitive properties such as the rms bond length fluctuations and diffusion constants that have been calculated in both the micro-canonical and canonical ensembles reveals more similarities than differences (the the temperature curves have roughly the same shape and differ primarily by their displacement in temperature) and again, one is left with the dilemma of justifying why the agreement between the Monte Carlo results and the molecular dynamics results is so poor for these clusters but so good for the other sizes.

Despite these inconsistencies, the bulk of my results are consistent with the view of a dynamic coexistence in the transition region and can be interpreted within that framework. My results are not totally inconsistent with the viewpoint that emphasizes the smooth progression of isomerizations between locally similar but globally distinct configurations occurring throughout the transition region. Clearly, cluster transitions are a progression of isomerizations — the issue is just how smooth these progressions really are. For clusters such as  $N = 15, 16$  and  $17$  the progressions appear to be very smooth, but for many other clusters (especially the magic number clusters), the threshold behavior of many of their properties and their very different heat capacity behavior implies an abruptness in the progressions that is more appropriately described then by the coexistence viewpoint.

The nature of cluster phase transitions still remains much unresolved then, despite the

additional information provided by the heat capacity results. More data is required to resolve the outstanding issues. This can be accomplished by extending the systematic survey of cluster properties beyond  $N = 24$ , but another avenue also seems appropriate. Since many cluster properties result from an interplay of particle dynamics based on coordinated atom moves, and structural effects based on particle size and intermolecular forces, the study of heterogeneous atomic clusters of various size and composition can help determine the relative importance of each factor. Work is currently underway on a J-walking study of binary Ne-Ar and Ar-Kr clusters. Ne and Ar differ greatly in both size and potential, but Ar and Kr have similar sizes and so differences in their behavior can provide more insight into the transition region.

#### ACKNOWLEDGMENTS

Support for this research by the Natural Sciences and Engineering Research Council of Canada (NSERC) is gratefully acknowledged. I also thank David L. Freeman for helpful discussions, and Richard M. Stratt for his comments.

## REFERENCES

- <sup>1</sup> T. L. Beck and R. S. Berry, J. Chem. Phys. **88**, 3910 (1988); J. Jellinek, T. L. Beck, and R. S. Berry, J. Chem. Phys. **84**, 2783 (1986).
- <sup>2</sup> D. J. Wales and R. S. Berry, J. Chem. Phys. **92**, 4283 (1990).
- <sup>3</sup> T. L. Beck, J. Jellinek, and R. S. Berry, J. Chem. Phys. **87**, 545 (1987).
- <sup>4</sup> R. S. Berry, T. L. Beck, H. L. Davis and J. Jellinek, in *Advances in Chemical Physics*, edited by I. Prigogine and S. A. Rice (Wiley, New York, 1988), Vol. 70B, p. 75.
- <sup>5</sup> H. Matsuoka, T. Hirokawa, M. Matsui, and M. Doyama, Phys. Rev. Lett. **69**, 297 (1992).
- <sup>6</sup> T. L. Beck and T. L. Marchioro II, J. Chem. Phys. **93**, 1347 (1990).
- <sup>7</sup> J. E. Adams and R. M. Stratt, J. Chem. Phys. **93**, 1332 (1990).
- <sup>8</sup> J. E. Adams and R. M. Stratt, J. Chem. Phys. **93**, 1632 (1990).
- <sup>9</sup> M. Bixon and J. Jortner, J. Chem. Phys. **91**, 1631, (1989).
- <sup>10</sup> I. L. Garzón and M. Avalos Borja, and Estela Blaisten-Borojas, Phys. Rev. B **40**, 4749 (1989).
- <sup>11</sup> J. D. Honeycutt and H. C. Andersen, J. Phys. Chem. **91**, 4950, (1987).
- <sup>12</sup> N. Quirke and P. Sheng, Chem. Phys. Lett. **110**, 63 (1984).
- <sup>13</sup> R. D. Etters and J. B. Kaelberer, J. Chem. Phys. **66**, 5112 (1977); J. B. Kaelberer and R. D. Etters, J. Chem. Phys. **66**, 3233 (1977).
- <sup>14</sup> R. D. Etters and J. B. Kaelberer, Phys. Rev. A **11**, 1068 (1975).
- <sup>15</sup> C. L. Briant and J. J. Burton, J. Chem. Phys. **63**, 2045 (1975).
- <sup>16</sup> J. K. Lee, J. A. Barker, and F. F. Abraham, J. Chem. Phys. **58**, 3166 (1973).
- <sup>17</sup> D. Eichenauer and R. J. Le Roy, Phys. Rev. Lett. **57**, 2920 (1986).

- <sup>18</sup> J. Farges, M. F. de Feraudy, B. Raoult, and G. Torchet, *J. Chem. Phys.* **78**, 5067 (1983).
- <sup>19</sup> O. Echt, K. Sattler, and R. Recknagel, *Phys. Rev. Lett.* **47**, 1121 (1981).
- <sup>20</sup> D. L. Freeman and J. D. Doll, *J. Chem. Phys.* **82**, 462 (1985).
- <sup>21</sup> N. Metropolis, A. Rosenbluth, M. N. Rosenbluth, A. Teller and E. Teller, *J. Chem. Phys.* **21**, 1087 (1953).
- <sup>22</sup> J. P. Valleau and S. G. Whittington, in *Statistical Mechanics*, edited by B. J. Berne (Plenum, New York, 1977), Ch. 4, p. 145.
- <sup>23</sup> M. H. Kalos and P. A. Whitlock, *Monte Carlo Methods* (Wiley, New York, 1986), Ch. 3, pp. 73–83.
- <sup>24</sup> M. P. Allen and D. J. Tildesley, *Computer Simulation of Liquids* (Clarendon Press, Oxford, 1987).
- <sup>25</sup> J. M. Haile, *Molecular Dynamics Simulation: Elementary Methods* (Wiley-Interscience, New York, 1992).
- <sup>26</sup> R. W. Hockney and J. W. Eastwood, *Computer Simulation using Particles* (Adam-Hilger, Bristol, 1988).
- <sup>27</sup> D. G. Vlachos, L. D. Schmidt, and R. Aris, *J. Chem. Phys.* **96**, 6880 (1992); **96**, 6891 (1992).
- <sup>28</sup> For reviews of recent work, see J. D. Doll, D. L. Freeman and T. L. Beck, in *Advances in Chemical Physics*, edited by I. Prigogine and S. A. Rice (Wiley, New York, 1990), Vol. 78, p. 61; D. L. Freeman and J. D. Doll, in *Advances in Chemical Physics*, edited by I. Prigogine and S. A. Rice (Wiley, New York, 1988), Vol. 70B, p. 139; B. J. Berne and D. Thirumalai, *Annu. Rev. Phys. Chem.* **37**, 401 (1986).
- <sup>29</sup> J. A. Northby, *J. Chem. Phys.* **87**, 6166 (1987).

- <sup>30</sup> M. R. Hoare and P. Pal, Adv. Phys. **20**, 161 (1971).
- <sup>31</sup> C. D. Maranas and C. A. Floudas, J. Chem. Phys. **97**, 7667 (1992).
- <sup>32</sup> C. J. Tsai and K. D. Jordan, J. Chem. Phys. **99**, 6957 (1993).
- <sup>33</sup> H. L. Davis, J. Jellinek, and R. S. Berry, J. Chem. Phys. **86**, 6456 (1987).
- <sup>34</sup> P. Labastie and R. L. Whetten, Phys. Rev. Lett. **65**, 1567 (1990).
- <sup>35</sup> V. V. Nauchitel and A. J. Pertsin, Mol. Phys. **40**, 1341 (1980).
- <sup>36</sup> J. Cao and B. J. Berne, J. Chem. Phys. **92**, 1980 (1990).
- <sup>37</sup> D. D. Frantz, D. L. Freeman, and J. D. Doll, J. Chem. Phys. **93**, 2769 (1990).
- <sup>38</sup> Gustavo E. Lopez and David. L. Freeman, J. Chem. Phys. **98**, 1428 (1993).
- <sup>39</sup> C. J. Tsai and K. D. Jordan, J. Chem. Phys. **95**, 3850 (1991).
- <sup>40</sup> M. A. Strozak, G.E. Lopez and D.L. Freeman, J. Chem. Phys. **97**, 4445 (1992).
- <sup>41</sup> See A. M. Ferrenberg and R. H. Swendsen, Comput. Phys. **3**(5), 101 (1989) and references therein.
- <sup>42</sup> D. D. Frantz, D. L. Freeman, and J. D. Doll, J. Chem. Phys. **97**, 5713 (1992).
- <sup>43</sup> Distributions were typically used until the jump acceptance dropped down to about 10%, although the values were often greater for the wider distributions in the high temperature dissociation region and lower for the narrower distributions in the low temperature solid region.
- <sup>44</sup> Calculations for cluster sizes  $N = 4$  to 8 were performed on a DECstation 5000/200 UNIX workstation equipped with 16 Mb of RAM. The memory was upgraded to 64 Mb for clusters  $N = 9$  to 16, and then upgraded again to 96 Mb for clusters  $N = 17$  to 19. Calculations for cluster sizes  $N = 20$ , 22 and 24 were performed on a DEC Alpha 3000/500 AXP equipped with 196 Mb of RAM. Calculations for cluster sizes  $N = 21$  and

23 were performed on a DEC Alpha 3000/300L AXP equipped with 32 Mb of RAM.

<sup>45</sup> The Savitsky-Golay algorithm was used for the data smoothing, and 2D cubic splines were used for the interpolation. These routines are implemented in the MS-DOS graphics software package Axum, version 3.0. Different fits were obtained by using different smoothing orders, corresponding to 7, 9, 11 or 13 surrounding data points being used to fit each point.

<sup>46</sup> The self diffusion constants as functions of temperature differed substantially from those obtained from molecular dynamics calculations by Beck and Marchioro (Ref. 6) by their lack of a sharp rise in the transition region. A subsequent instantaneous normal mode analysis by Adams and Stratt (Ref. 8) using an expression for the diffusion constant that was more sensitive to the low frequency part of the phonon spectrum gave results that were in agreement with the molecular dynamics calculations. The curves for Ar<sub>7</sub> and Ar<sub>8</sub> remained very much alike.

<sup>47</sup> Because the J-walking runs were started at high temperatures from random configurations, and the temperatures were decreased in small increments down to zero, the simulations also served as global minimization calculations, akin to simulated annealing. In all cases, the lowest energy configuration obtained with J-walking was the same as that reported in Refs. 29 and 31.

<sup>48</sup> R. M. Stratt, private communication.



## FIGURES

FIG. 1. Classical internal energy (at left) and constant volume heat capacity (at right) as functions of temperature for  $\text{Ar}_{23}$  clusters; both are in reduced units, with  $U^* = U/\epsilon$  and  $C_V^* = C_V/k_B$ . The lower temperature heat capacity peak corresponds to a solid-liquid transition, while the higher temperature peak corresponds to a liquid-vapor transition. The solid curves were obtained using J-walking from external J-walker distributions containing  $10^6$  configurations; the jump attempt frequency was  $P_J = 0.1$ . For each temperature,  $10^5$  warmup passes were run, followed by  $10^7$  passes with data accumulation. The dashed curves were obtained using standard Metropolis Monte Carlo methods, likewise consisting of  $10^5$  warmup passes followed by  $10^7$  passes with data accumulation. Some representative single standard deviation error bars have been included. Also included in the heat capacity plot are results from Metropolis runs consisting of  $10^5$  warmup passes followed by  $10^5$  passes with data accumulation (curve i) and  $10^6$  passes with data accumulation (curve ii). Lack of convergence in the Metropolis simulations is evident in the solid-liquid transition region.

FIG. 2. Normalized potential energy histograms for  $N = 11$  and  $N = 19$  J-walker distributions. Distribution particulars are given in Tables I and II. As the cluster size increases, so does the potential energy range, implying more distributions are required to span the entire range.

FIG. 3. The dependence on walk length for Metropolis averages of the rms bond length fluctuations  $\delta$  as a function of temperature for  $N = 13$ . The values at each temperature are averages obtained from 10 Metropolis Monte Carlo walks having lengths of  $10^4$  passes (short dashes),  $10^5$  passes (long dashes) and  $10^6$  passes (solid line). The dotted curve is the heat capacity from Fig. 5, and has been included for comparison. Slow convergence due to quasi-ergodicity in the transition region is evident by the displacement of the curves to lower temperatures with increased walk length. The insert shows the temperature  $T_\delta^* = 0.173$  where the rms bond length fluctuations begin to rise sharply. The solid triangle indicates the temperature  $T_{\delta, \text{MD}}^*$  where the rms bond length fluctuations obtained from molecular dynamics simulations reported in Ref. 3 were found to rise sharply.

FIG. 4. Heat capacity curves as functions of temperature (upper curves in each plot, in reduced units) for clusters ranging from  $N = 4$  to 12. All curves were obtained using J-walking from externally stored J-walker distributions with jumps attempted with a frequency of  $P_J = 0.1$ . The distribution parameters are listed in Table I. For each temperature, simulations consisted of  $10^5$  warmup passes followed by  $10^7$  passes with data accumulation. The lower, noisy curves are heat capacity standard deviations obtained from similar Metropolis Monte Carlo simulations, each consisting of  $10^5$  warmup passes followed by  $10^7$  passes with data accumulation. The temperatures corresponding to a sudden increase in standard deviation (indicated by the arrows) serve as estimates to the beginning of the solid-liquid transition regions. For those clusters having heat capacity curves with peaks in the solid-liquid transition region ( $N = 6, 9-12$ ), the temperatures corresponding to the low temperature side inflection point,  $T_L^*$ , the peak,  $T_P^*$ , and the high temperature side local minimum,  $T_H^*$  are indicated on the temperature axis by the large ticks. For  $N = 7$ , which has a shoulder in its heat capacity curve in this region, the large ticks indicate the inflection points,  $T_L^*$  and  $T_H^*$ . These peak parameters are also listed in Table III. For those clusters having molecular dynamics simulations reported in Ref. 3 ( $N = 7-9$  and 11), the solid triangles indicate the temperatures at which the rms bond length fluctuations  $\delta$  were found to rise sharply, while the horizontal error bars represent the coexistence temperature ranges,  $\Delta T_c^* = T_m^* - T_f^*$ , for those clusters found to have a bimodal form in the distribution of short-time averaged kinetic energies.

FIG. 5. Same as Fig. 4, but for clusters ranging in size from  $N = 13$  to 24. The J-walker distribution parameters are listed in Table II.

FIG. 6. Magic number effects in cluster heat capacities. The top plot shows the solid-liquid transition region heat capacity peak characteristic temperatures as functions of cluster size  $N$ . For those clusters having distinct peaks, the values  $T_L^*$ ,  $T_P^*$  and  $T_H^*$  are indicated, while for those clusters having heat capacity shoulders in this region,  $T_P^*$  is taken to be  $T_H^*$ . These points are also indicated in Figs. 4 and 5 by the large ticks on the temperature axes. No solid-liquid transition region heat capacity peaks or shoulders were found for  $N = 4, 5$  and  $8$ . The lower  $T_\sigma^*$  curve indicates the dependence on cluster size for the beginning of the transition region (also indicated by the arrows in Figs. 4 and 5). The solid-liquid transition ranges can be defined as the difference between the top and the bottom curves,  $\Delta T^* = T_H^* - T_\sigma^*$ . The middle plot shows the size dependence on the corresponding heat capacities. The bottom plot was inspired by Ref. 29 and has been included for comparison. It plots the binding energy differences between successive clusters, as a function of size,  $\Delta E_b(N) = -\Delta V_{\min}(N) = -[V_{\min}(N) - V_{\min}(N - 1)]$ . Magic number sizes based on zero temperature structural stability ( $N = 13, 19$  and  $23$ , and to a lesser extent,  $N = 7$ ) have a clear correlation with those evident in the heat capacity peaks.

FIG. 7. Rms bond length fluctuations as functions of temperature for  $N = 4-9$ . The values at each temperature are averages obtained from 10 Metropolis Monte Carlo walks having lengths of  $10^6$  passes. Some representative single standard deviation error bars have been included. Only the  $N = 4$  curve shows no abrupt change in the solid-liquid region before rising sharply in the dissociation region. The  $N = 7$  curve shows magic number behavior that reflects the enhanced stability of the cluster's lowest energy configuration. Its sharp rise occurs at a much higher temperature than that for either  $N = 6$  or  $N = 8$ .

FIG. 8. Pentagonal “auf-bau” in the minimum energy configurations for Lennard-Jones clusters. The configurations shown are the lowest energy isomers obtained from the J-walking simulations, and are identical to those found in other studies.<sup>29–31</sup> Beginning with the pentagonal bipyramid core corresponding to  $N = 7$ , the minimum energy configuration for each succeeding cluster up to  $N = 12$  can be formally obtained by adding an atom (indicated by the shading) to a neighboring pentagonal site to form a second five-atom ring, which is then capped to form the  $N = 13$  icosahedron. Except for  $N = 17$ , the minimum energy configurations for  $N = 14$  to 19 are analogous, with succeeding clusters built up from the icosahedral core by adding an atom to a neighboring pentagonal site to form a third five-atom ring, which is then capped to form the  $N = 19$  double icosahedron. This correspondence between clusters  $N = 8$  to 13 and  $N = 14$  to 19 is reflected in the binding energy differences,  $\Delta E_b$ , shown in Fig. 6 — the sequence for  $N = 8$  to 13 is nearly identical with the sequence for  $N = 14$  to 19.

FIG. 9. Rms bond length fluctuations as functions of temperature for  $N = 13$ –15 and  $N = 19$ –21. The values were obtained in the same manner as those in Fig. 7. Magic number behavior is also evident for  $N = 13$  and  $N = 19$  by their significantly higher temperatures marking the onset of the sharp rise in  $\delta(T)$ . The  $N = 14$  curve is somewhat unusual, showing a smaller, nearly linear rise at about  $T^* = 0.064$  until about  $T^* = 0.13$  where it then undergoes the sharp rise typical of the other clusters.

FIG. 10. Minimum energy configurations for  $N = 20$  to 24. The configurations shown are the lowest energy isomers obtained from the J-walking simulations, and are identical to those found in other studies.<sup>29,31</sup> Each configuration can be obtained formally from the preceding one by the addition of the shaded atom. For  $N = 23$ , the additional atom caps an interpenetrating icosahedral substructure, forming a magic number structure.

FIG. 11. Potential energy curves as functions of temperature obtained from J-walking simulations for clusters ranging from  $N = 4$  (top curve) to  $N = 24$  (bottom curve). The magic number sizes ( $N = 7, 13, 19$  and  $23$ ) are indicated by the dashed curves. Reduced units have been used, with  $V^* = V/\epsilon$  and  $T^* = k_B T/\epsilon$ . The dotted lines intersecting the curves are the values for the beginning of the transition region  $T_\sigma^*$  (as characterized by a sharp rise in the heat capacity fluctuations), and the solid-liquid transition region heat capacity peak characteristic temperatures ( $T_L^*$ ,  $T_P^*$  and  $T_H^*$  for clusters having distinct peaks, or the inflection points  $T_L^*$  and  $T_H^*$  for those clusters having heat capacity shoulders). The transformation from the solid-like region to the liquid-like region is evident by the change in spacing between the curves from nonuniform at low temperatures to nearly uniform at high temperatures.

FIG. 12. Potential energy differences as functions of temperature  $T^*$  and size  $N$  (the vertical axis is  $-\Delta\langle V(N, T) \rangle = -[\langle V_N(T) \rangle - \langle V_{N-1}(T) \rangle]$ ). The temperature mesh size is  $\Delta T = 0.2$  K, or  $\Delta T^* = 0.00562$ . The structure of the zero temperature curve  $\Delta E_b(N)$  (which is also shown in Fig. 6) can be seen to extend well into the transition regions, indicating the persistence of the solid-like lowest energy isomer, especially for the magic number sizes. The dashed curves correspond to the temperatures closest to the heat capacity peak temperatures  $T_P^*$  for the magic numbers  $N = 13$  (long dashes),  $19$  (medium dashes) and  $23$  (short dashes).

FIG. 13. Normalized potential energy distribution surfaces as functions of potential energy and temperature for  $N = 13$  to  $18$ . The surfaces are comprised of potential energy histograms obtained from J-walking simulations with temperature increments of  $\Delta T = 0.2$  K ( $\Delta T^* = 0.00562$ ). In each case, the truncated peak on the left represents the solid region and the peak on the right the dissociation region; saddle points correspond to heat capacity peaks.

FIG. 14. Normalized potential energy histograms for temperatures near the solid-liquid transition region heat capacity peak for the magic number clusters. The solid curves are for temperatures below  $T_P^*$ , the dotted curves for temperatures above; the temperature increment is  $\Delta T = 0.1$  K ( $\Delta T^* = 0.00281$ ). The data was obtained from the J-walking simulations. Only the  $N = 13$  distributions have a bimodal form indicative of solid-liquid coexistence.

FIG. 15. Magic number effects in cluster rms bond length fluctuations. The plot shows the temperatures  $T_{\delta,MC}^*$ , where  $\delta(T)$  obtained from Metropolis simulations begins to deviate sharply from the nearly linear increase associated with the solid region (see Fig. 3 for an example). For  $N = 14, 18, 22$  and  $24$ , the lower triangle signifies the temperature where  $\delta(T)$  first has a moderate rise at the end of the solid region, and the upper triangle signifies temperature where  $\delta(T)$  then rises sharply. Also shown are the corresponding values  $T_{\delta,MD}^*$  obtained from molecular dynamics simulations reported in Ref. 3; the vertical error bars indicate the coexistence ranges found in the molecular dynamics studies. The Metropolis values occur at much lower temperatures, but show a similar pattern as a function of size. Also included are the heat capacity peak temperatures  $T_P^*$  and the transition ranges  $\Delta T^* = T_H^* - T_\sigma^*$ , which are indicated by the dotted lines. The temperatures  $T_{\delta,MC}^*$  can be seen to roughly correspond to the beginning of the transition ranges  $T_\sigma^*$  for most sizes.

# TABLES

TABLE I. J-walker distributions for  $4 \leq N \leq 12$ . The distributions for each cluster were generated in stages, with the initial J-walker distribution obtained from a single Metropolis walk at a temperature high enough to be in the cluster dissociation region, and subsequent lower temperature distributions obtained using J-walking from the preceding distribution; the jump attempt frequency was  $P_J = 0.1$  throughout. For each distribution,  $10^6$  warmup moves were made before configurations were stored. All distributions consisted of  $10^6$  configurations stored in 10 or 50 files (depending on the amount of computer primary memory), except for  $N = 4$  and  $N = 8$ , which had  $1.25 \times 10^6$  and  $0.75 \times 10^6$  configurations, respectively. Configurations were stored periodically at intervals of  $J_{\text{extra}}$  moves. For those distributions obtained using J-walking,  $\%J_A$  gives the percentage of attempted jumps that were accepted. Absolute temperatures are for Ne. Potential energy histograms for the  $N = 11$  distributions are shown in Figure 2.

$N = 4$				$N = 5$				$N = 6$			
$T(\text{K})$	$T^*$	$J_{\text{extra}}$	$\%J_A$	$T(\text{K})$	$T^*$	$J_{\text{extra}}$	$\%J_A$	$T(\text{K})$	$T^*$	$J_{\text{extra}}$	$\%J_A$
15.0	0.421	400		20.0	0.562	500		15.0	0.421	600	
8.0	0.225	400	8.1	11.0	0.309	500	33.4	12.0	0.337	600	43.4
4.0	0.112	400	12.4	7.0	0.197	500	4.4	8.0	0.225	600	5.0
								4.0	0.112	600	8.6
$N = 7$				$N = 8$				$N = 9$			
$T(\text{K})$	$T^*$	$J_{\text{extra}}$	$\%J_A$	$T(\text{K})$	$T^*$	$J_{\text{extra}}$	$\%J_A$	$T(\text{K})$	$T^*$	$J_{\text{extra}}$	$\%J_A$
15.0	0.421	1000		20.0	0.562	800		20.0	0.562	900	
12.0	0.337	1000	18.2	15.0	0.421	800	45.9	15.0	0.421	900	28.1
8.0	0.225	1000	9.1	12.0	0.337	800	9.3	11.5	0.323	900	7.1
				8.0	0.225	800	11.1	7.0	0.197	900	6.2
$N = 10$				$N = 11$				$N = 12$			

$T(\text{K})$	$T^*$	$J_{\text{extra}}$	$\%J_A$	$T(\text{K})$	$T^*$	$J_{\text{extra}}$	$\%J_A$	$T(\text{K})$	$T^*$	$J_{\text{extra}}$	$\%J_A$
20.0	0.562	1000		20.0	0.562	1000		20.0	0.562	1200	
16.0	0.449	1000	34.2	16.0	0.449	1100	19.8	17.0	0.478	1200	30.8
12.0	0.337	1000	4.4	12.0	0.337	1100	6.2	14.0	0.393	1200	13.1
8.0	0.225	1000	9.6	8.0	0.225	1100	7.6	10.0	0.281	1200	7.2
5.0	0.140	1000	6.5	5.0	0.140	1100	5.9	7.0	0.197	1200	8.6
								4.0	0.112	1200	6.5



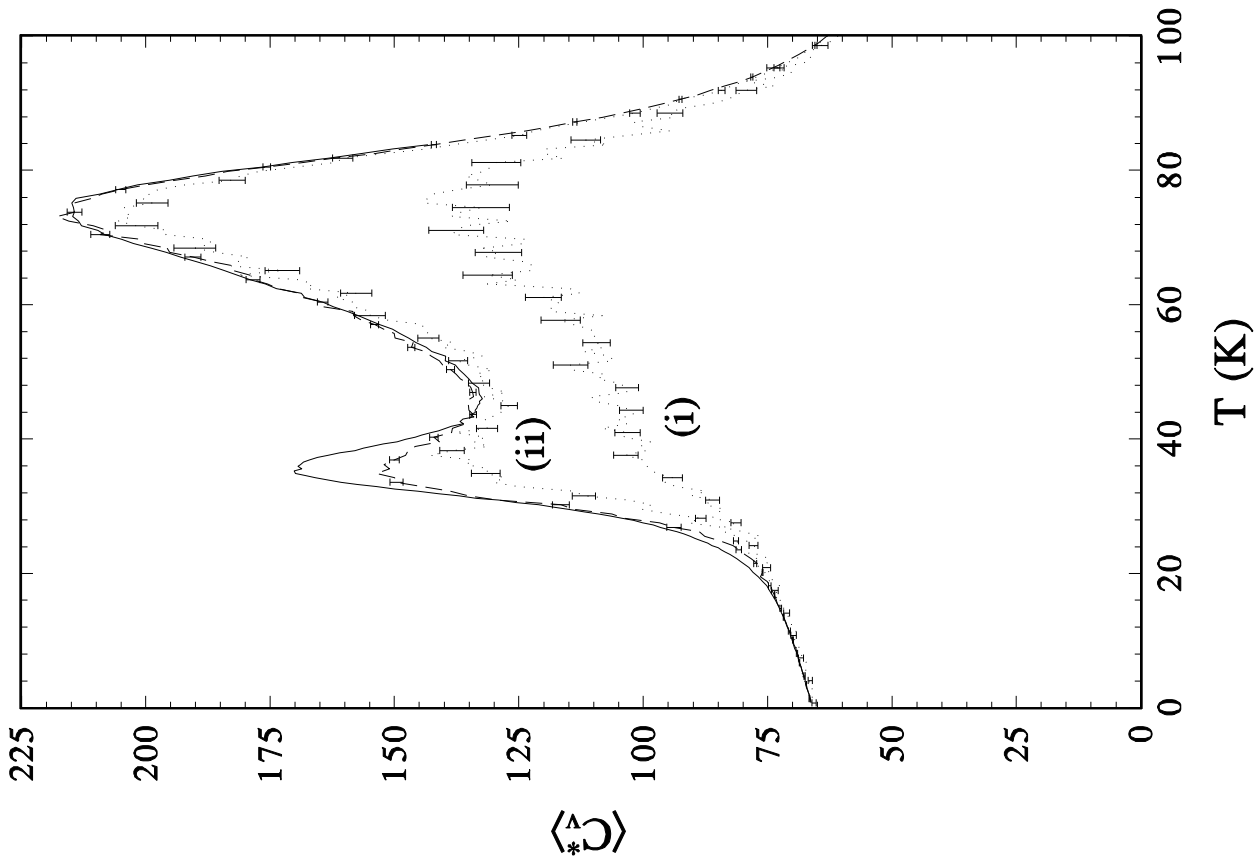
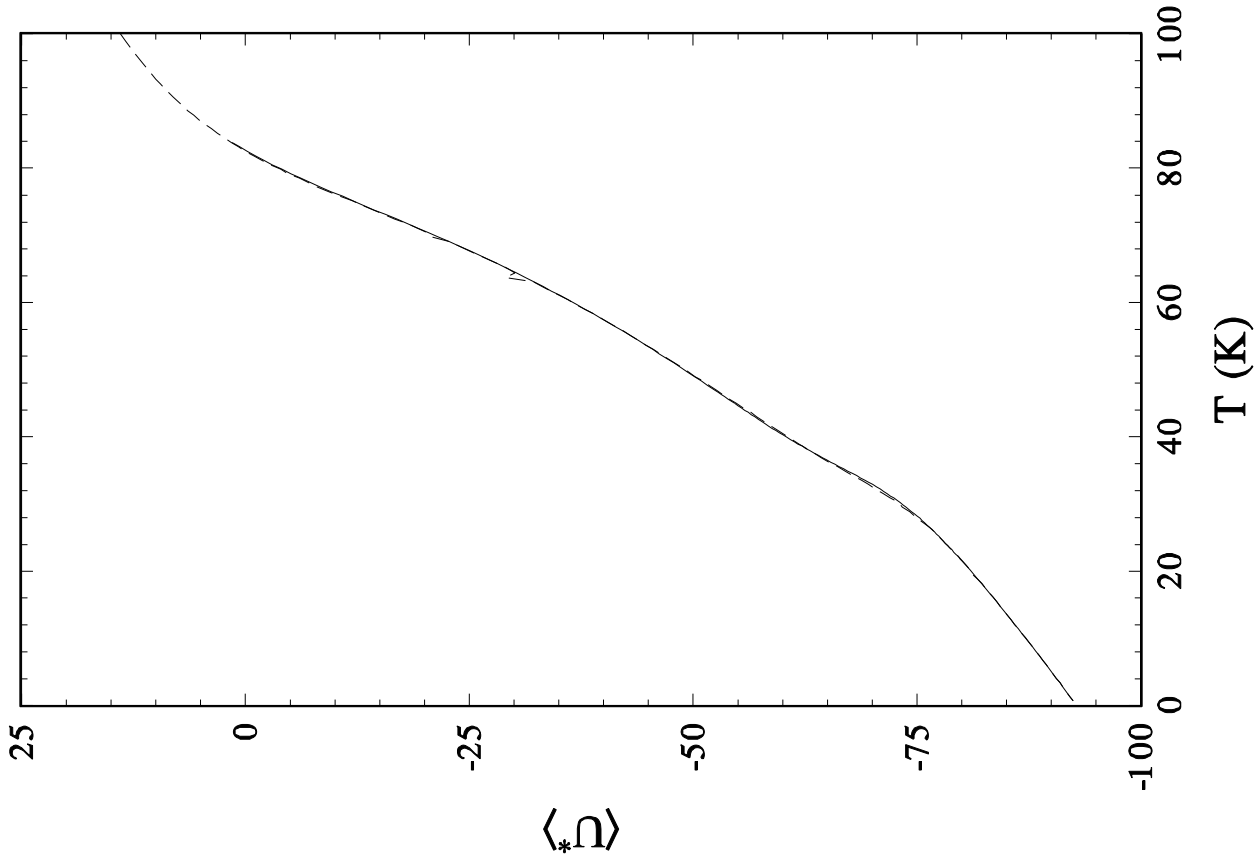
TABLE II. J-walker distributions for  $13 \leq N \leq 24$ . The distributions were obtained as described in Table I. Potential energy histograms for the  $N = 19$  distributions are shown in Figure 2.

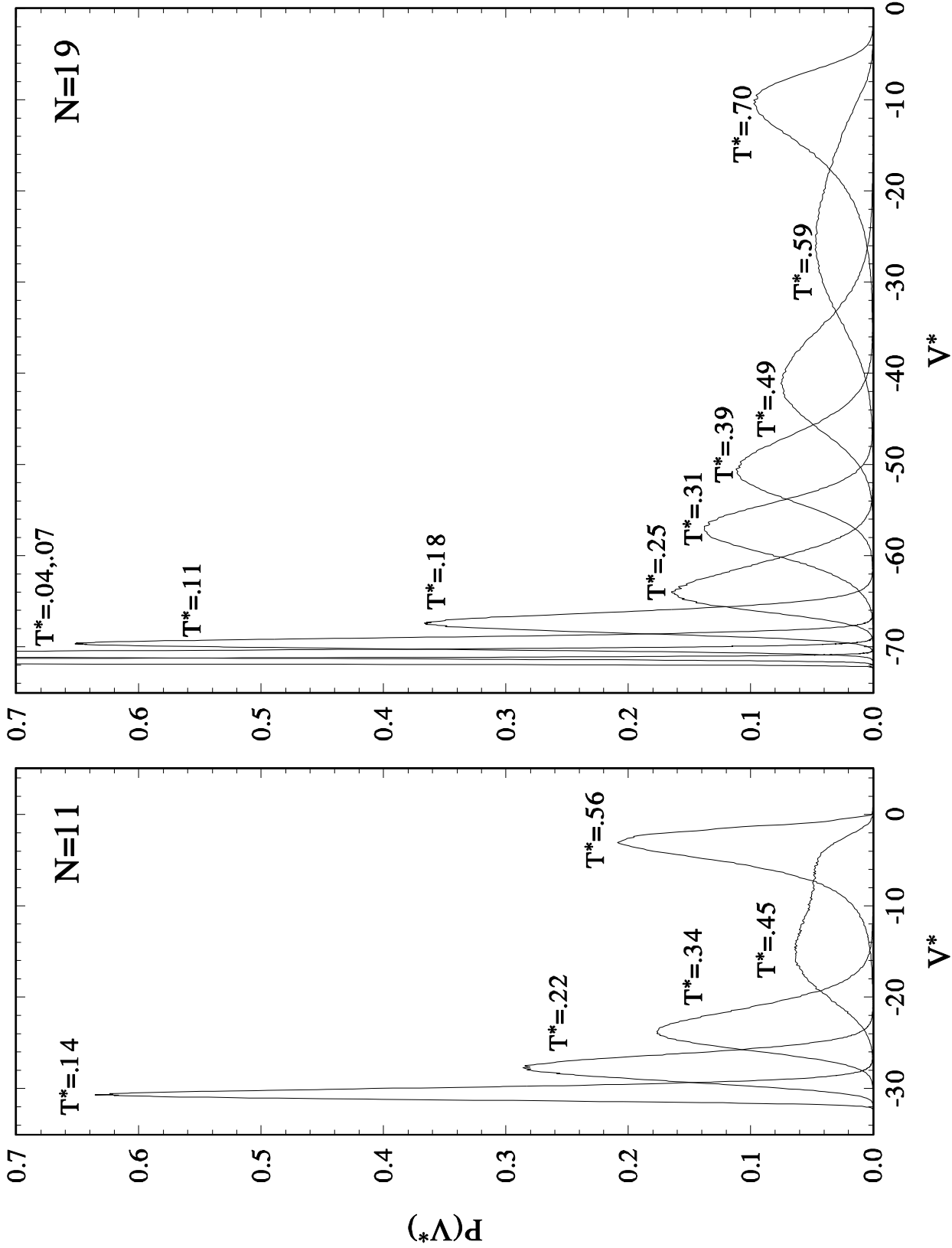
$N = 13$				$N = 14$				$N = 15$				$N = 16$			
$T(K)$	$T^*$	$J_{\text{extra}}$	$\%J_A$	$T(K)$	$T^*$	$J_{\text{extra}}$	$\%J_A$	$T(K)$	$T^*$	$J_{\text{extra}}$	$\%J_A$	$T(K)$	$T^*$	$J_{\text{extra}}$	$\%J_A$
22.0	0.618	1300		22.0	0.618	1400		25.0	0.702	1500		25.0	0.702	800	
18.0	0.506	1300	28.2	18.0	0.506	1400	18.3	21.0	0.590	1500	49.6	20.0	0.562	1600	23.0
14.0	0.393	1300	5.0	14.0	0.393	1400	6.0	17.5	0.492	1500	11.6	16.5	0.463	1600	9.0
10.5	0.295	1300	8.4	10.0	0.281	1400	3.8	14.0	0.393	1500	11.2	13.0	0.463	1600	11.5
7.0	0.197	1300	4.3	6.0	0.169	1400	2.8	11.0	0.309	1500	13.5	10.0	0.281	800	12.3
4.0	0.112	130	6.5	3.0	0.084	140	2.0	8.0	0.225	150	8.5	7.0	0.197	400	6.0
2.0	0.056	130	3.6					6.0	0.169	150	20.5	4.5	0.126	160	7.3
								4.0	0.112	150	13.5	2.5	0.070	160	3.9
								2.0	0.056	150	2.2				
$N = 17$				$N = 18$				$N = 19$				$N = 20$			
$T(K)$	$T^*$	$J_{\text{extra}}$	$\%J_A$	$T(K)$	$T^*$	$J_{\text{extra}}$	$\%J_A$	$T(K)$	$T^*$	$J_{\text{extra}}$	$\%J_A$	$T(K)$	$T^*$	$J_{\text{extra}}$	$\%J_A$
25.0	0.702	850		25.0	0.702	900		25.0	0.702	950		25.0	0.702	1000	
21.0	0.590	1700	33.9	21.0	0.590	1800	26.0	21.0	0.590	1900	20.8	21.0	0.590	2000	16.6
18.0	0.506	1700	15.3	18.0	0.506	1800	15.8	17.5	0.492	1900	10.7	17.5	0.492	2000	11.3
15.0	0.421	1700	17.7	15.0	0.421	1800	17.8	14.0	0.393	1900	11.6	14.0	0.393	2000	11.3
12.0	0.337	850	16.4	12.0	0.337	900	15.8	11.0	0.309	1900	12.2	11.0	0.309	2000	11.2
9.0	0.253	850	9.3	9.0	0.253	900	7.6	9.0	0.253	950	14.0	9.0	0.253	1000	13.9
6.5	0.183	170	9.5	6.5	0.183	900	9.2	6.5	0.183	950	9.3	6.5	0.183	1000	9.6
4.5	0.126	170	13.4	4.0	0.112	180	4.6	4.0	0.112	190	5.1	4.5	0.126	200	11.9
3.0	0.084	170	13.4	2.5	0.070	180	7.1	2.5	0.070	190	7.4	3.0	0.084	200	10.7
1.5	0.042	170	1.5	1.5	0.042	180	6.0	1.5	0.042	190	6.0	2.0	0.056	200	11.9
												1.0	0.028	200	1.0
$N = 21$				$N = 22$				$N = 23$				$N = 24$			
$T(K)$	$T^*$	$J_{\text{extra}}$	$\%J_A$	$T(K)$	$T^*$	$J_{\text{extra}}$	$\%J_A$	$T(K)$	$T^*$	$J_{\text{extra}}$	$\%J_A$	$T(K)$	$T^*$	$J_{\text{extra}}$	$\%J_A$
25.0	0.702	1050		25.0	0.702	1100		25.0	0.702	1150		25.0	0.702	1200	
21.0	0.590	2100	13.6	21.0	0.590	2200	11.9	21.0	0.590	2300	10.8	22.0	0.618	2400	23.7
17.5	0.492	2100	11.7	17.5	0.492	2200	11.8	18.0	0.506	2300	18.3	19.0	0.534	2400	18.7
14.0	0.393	2100	10.9	14.0	0.393	2200	10.5	15.0	0.421	2300	17.1	16.0	0.449	2400	16.9
11.0	0.309	2100	10.0	11.0	0.309	1100	9.6	12.5	0.351	2300	20.2	13.0	0.365	2400	14.0
8.5	0.239	1050	8.4	8.5	0.239	1100	7.4	10.5	0.295	2300	17.2	10.5	0.295	2400	11.3
6.0	0.169	1050	7.9	6.0	0.169	1100	7.4	8.5	0.239	1150	13.0	8.5	0.239	1200	12.5
4.0	0.112	210	8.1	4.0	0.112	220	7.3	6.5	0.183	230	16.4	6.5	0.183	1200	15.0
2.5	0.070	210	5.9	2.5	0.070	220	5.1	4.5	0.126	230	9.9	4.5	0.126	240	8.7
1.5	0.042	210	4.6	1.5	0.042	220	4.1	3.0	0.084	230	8.5	3.0	0.084	240	7.7

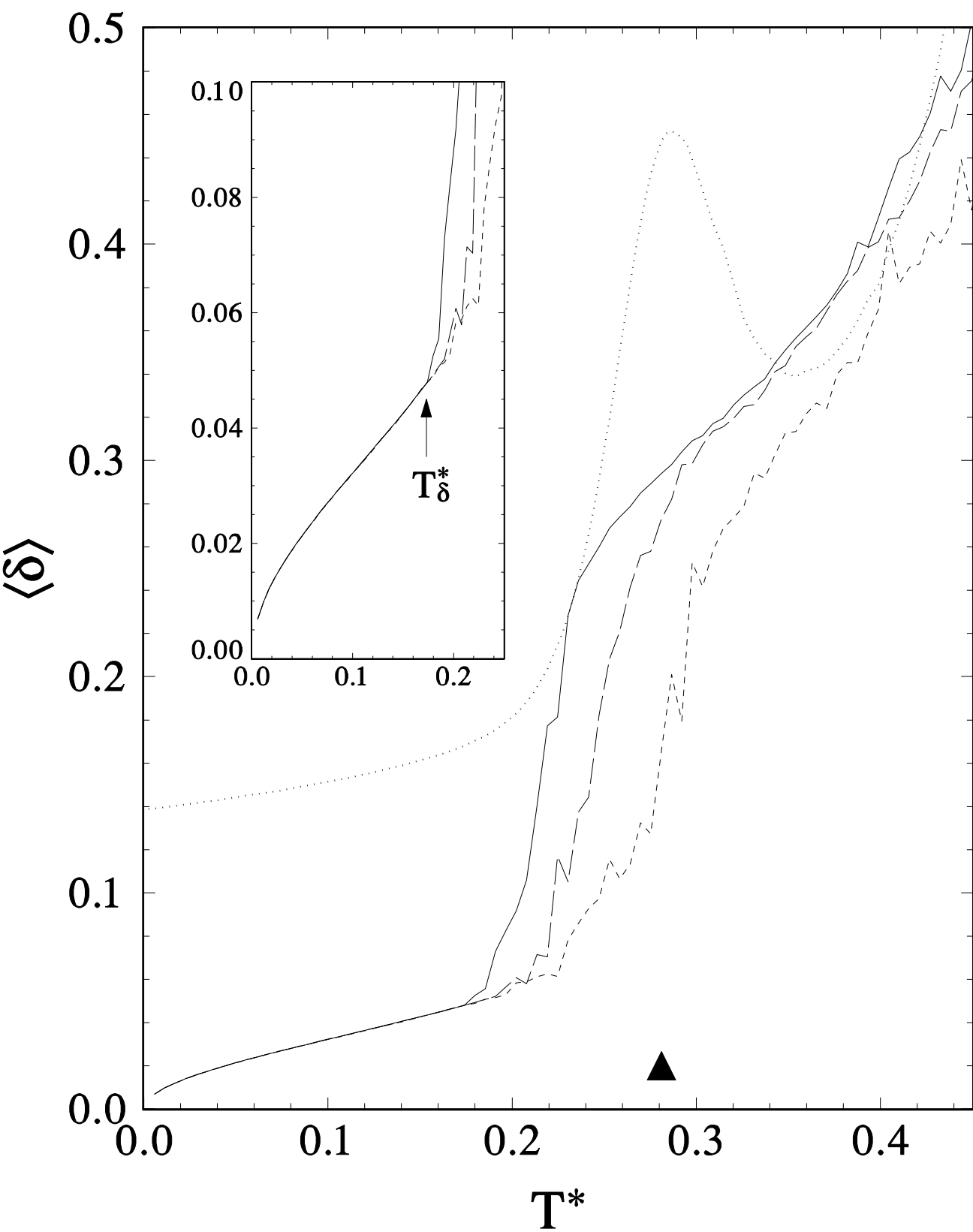
2.0	0.056	230	9.3	2.0	0.056	240	8.6
1.0	0.028	230	0.5	1.0	0.028	240	0.4

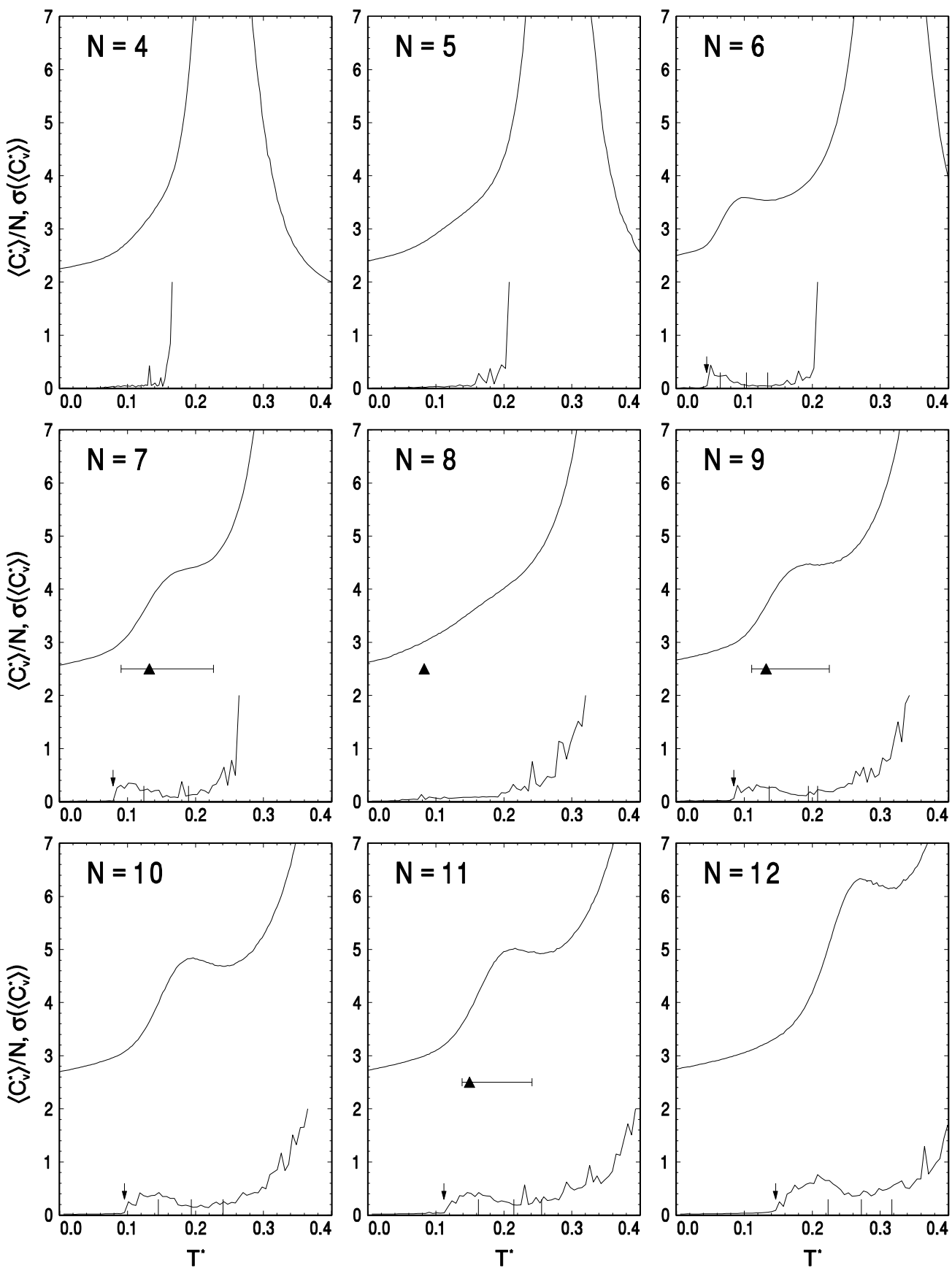
TABLE III. Solid-liquid transition region heat capacity peak parameters for  $4 \leq N \leq 24$ . These values were obtained by smoothing and interpolating the J-walking data shown in Figs. 4 and 5. The points  $(T_P^*, \langle C_V^* \rangle_P / N)$  are the heat capacity peaks, while the points  $(T_H^*, \langle C_V^* \rangle_H / N)$  are the local minima occurring on the high temperature side of each peak. For those clusters having heat capacity shoulders instead of peaks ( $N = 7, 15-17$ ), the points  $(T_H^*, \langle C_V^* \rangle_H / N)$  are the inflection points. The points  $(T_L^*, \langle C_V^* \rangle_L / N)$  are the inflection points on the low temperature side of the peak. The uncertainty estimates are standard deviations of the values obtained using different curve smoothing parameters.

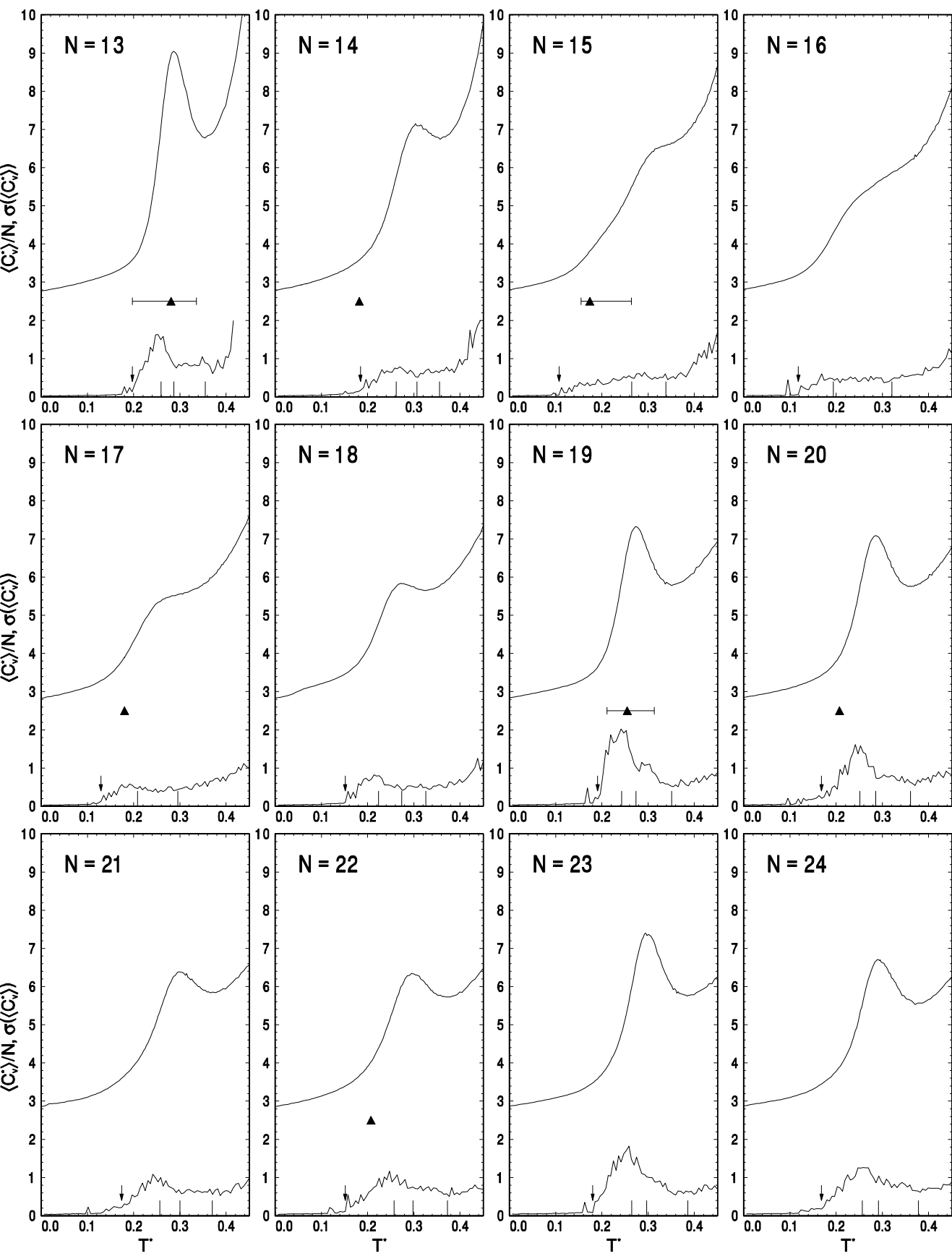
N	$T_L^*$		$\langle C_V^* \rangle_L / N$		$T_P^*$		$\langle C_V^* \rangle_P / N$		$T_H^*$		$\langle C_V^* \rangle_H / N$	
4												
5												
6	0.0652	$\pm 0.0004$	3.112	$\pm 0.008$	0.1036	$\pm 0.0008$	3.595	$\pm 0.001$	0.1344	$\pm 0.0003$	3.540	$\pm 0.002$
7	0.125	$\pm 0.002$	3.61	$\pm 0.04$					0.190	$\pm 0.004$	4.39	$\pm 0.01$
8												
9	0.137	$\pm 0.002$	3.81	$\pm 0.04$	0.1943	$\pm 0.0006$	4.470	$\pm 0.002$	0.208	$\pm 0.001$	4.455	$\pm 0.002$
10	0.145	$\pm 0.002$	3.99	$\pm 0.06$	0.1942	$\pm 0.0008$	4.834	$\pm 0.001$	0.240	$\pm 0.002$	4.687	$\pm 0.001$
11	0.162	$\pm 0.002$	4.18	$\pm 0.05$	0.215	$\pm 0.001$	5.010	$\pm 0.002$	0.255	$\pm 0.001$	4.925	$\pm 0.003$
12	0.224	$\pm 0.004$	5.0	$\pm 0.2$	0.272	$\pm 0.002$	6.326	$\pm 0.003$	0.317	$\pm 0.001$	6.146	$\pm 0.001$
13	0.2593	$\pm 0.0006$	7.10	$\pm 0.06$	0.2875	$\pm 0.0007$	9.06	$\pm 0.01$	0.3553	$\pm 0.0008$	6.794	$\pm 0.004$
14	0.263	$\pm 0.002$	5.8	$\pm 0.1$	0.307	$\pm 0.001$	7.124	$\pm 0.002$	0.356	$\pm 0.001$	6.770	$\pm 0.002$
15	0.265	$\pm 0.002$	5.52	$\pm 0.04$					0.339	$\pm 0.002$	6.589	$\pm 0.007$
16	0.194	$\pm 0.001$	4.29	$\pm 0.03$					0.321	$\pm 0.003$	5.86	$\pm 0.02$
17	0.209	$\pm 0.004$	4.5	$\pm 0.1$					0.295	$\pm 0.002$	5.538	$\pm 0.006$
18	0.224	$\pm 0.002$	4.80	$\pm 0.06$	0.274	$\pm 0.001$	5.834	$\pm 0.001$	0.326	$\pm 0.002$	5.652	$\pm 0.002$
19	0.243	$\pm 0.001$	5.92	$\pm 0.08$	0.2739	$\pm 0.0006$	7.318	$\pm 0.002$	0.352	$\pm 0.002$	5.794	$\pm 0.005$
20	0.2519	$\pm 0.0004$	5.77	$\pm 0.02$	0.2858	$\pm 0.0003$	7.085	$\pm 0.001$	0.3610	$\pm 0.0008$	5.756	$\pm 0.001$
21	0.257	$\pm 0.002$	5.37	$\pm 0.06$	0.300	$\pm 0.002$	6.383	$\pm 0.005$	0.371	$\pm 0.001$	5.843	$\pm 0.001$
22	0.258	$\pm 0.003$	5.5	$\pm 0.1$	0.298	$\pm 0.001$	6.333	$\pm 0.002$	0.3727	$\pm 0.0009$	5.726	$\pm 0.001$
23	0.265	$\pm 0.001$	6.05	$\pm 0.07$	0.297	$\pm 0.001$	7.383	$\pm 0.003$	0.386	$\pm 0.001$	5.764	$\pm 0.001$
24	0.257	$\pm 0.001$	5.56	$\pm 0.06$	0.2917	$\pm 0.0002$	6.703	$\pm 0.001$	0.3787	$\pm 0.0006$	5.557	$\pm 0.007$



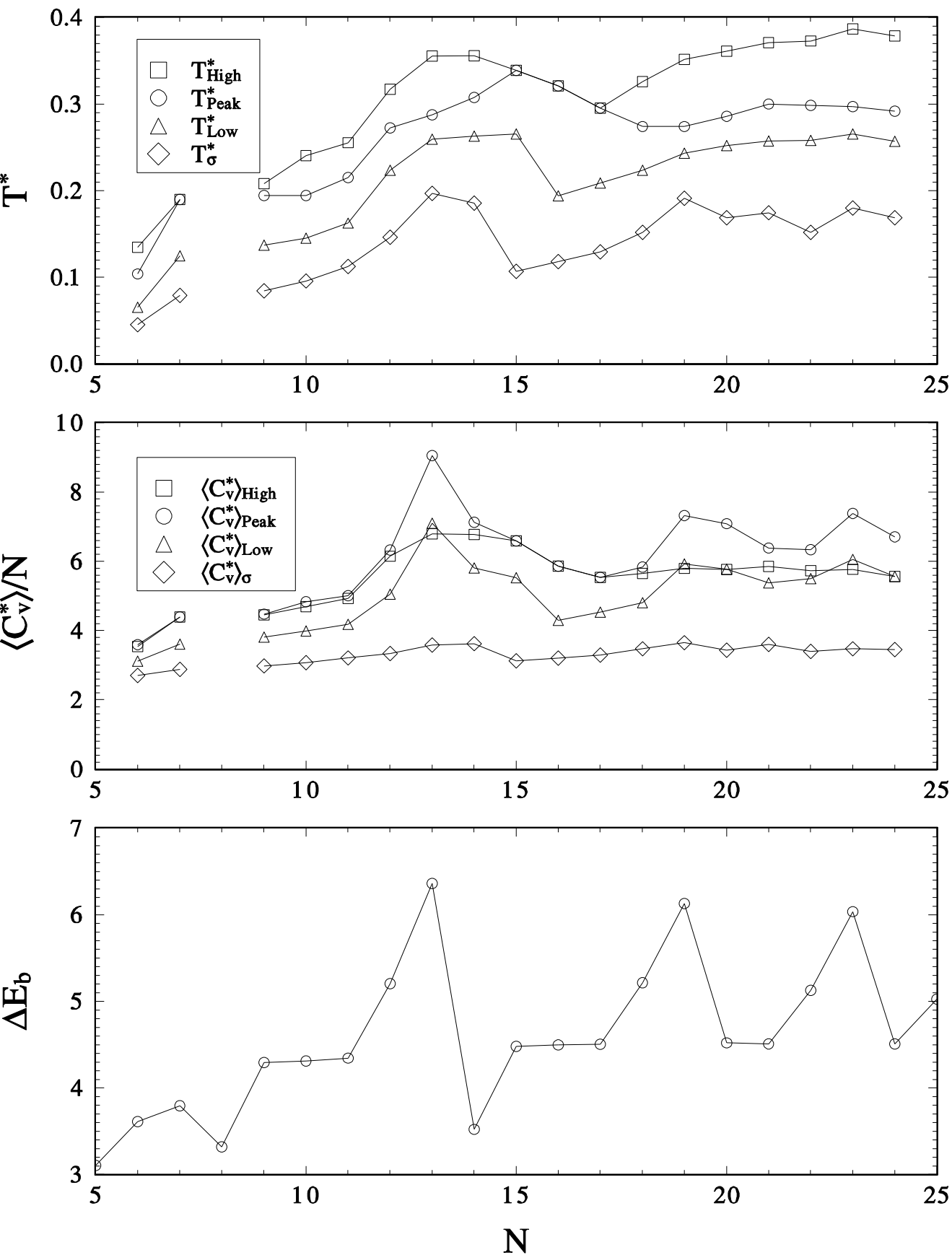


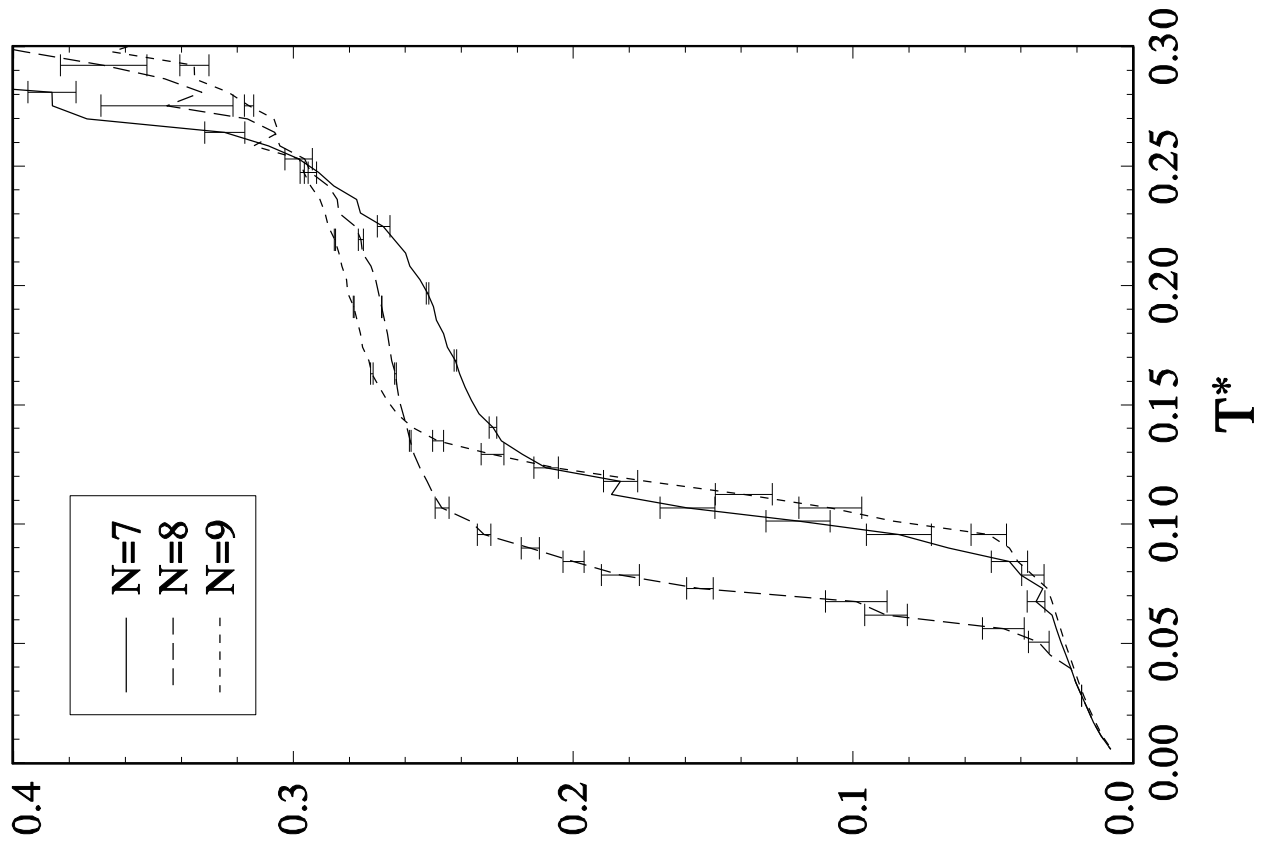
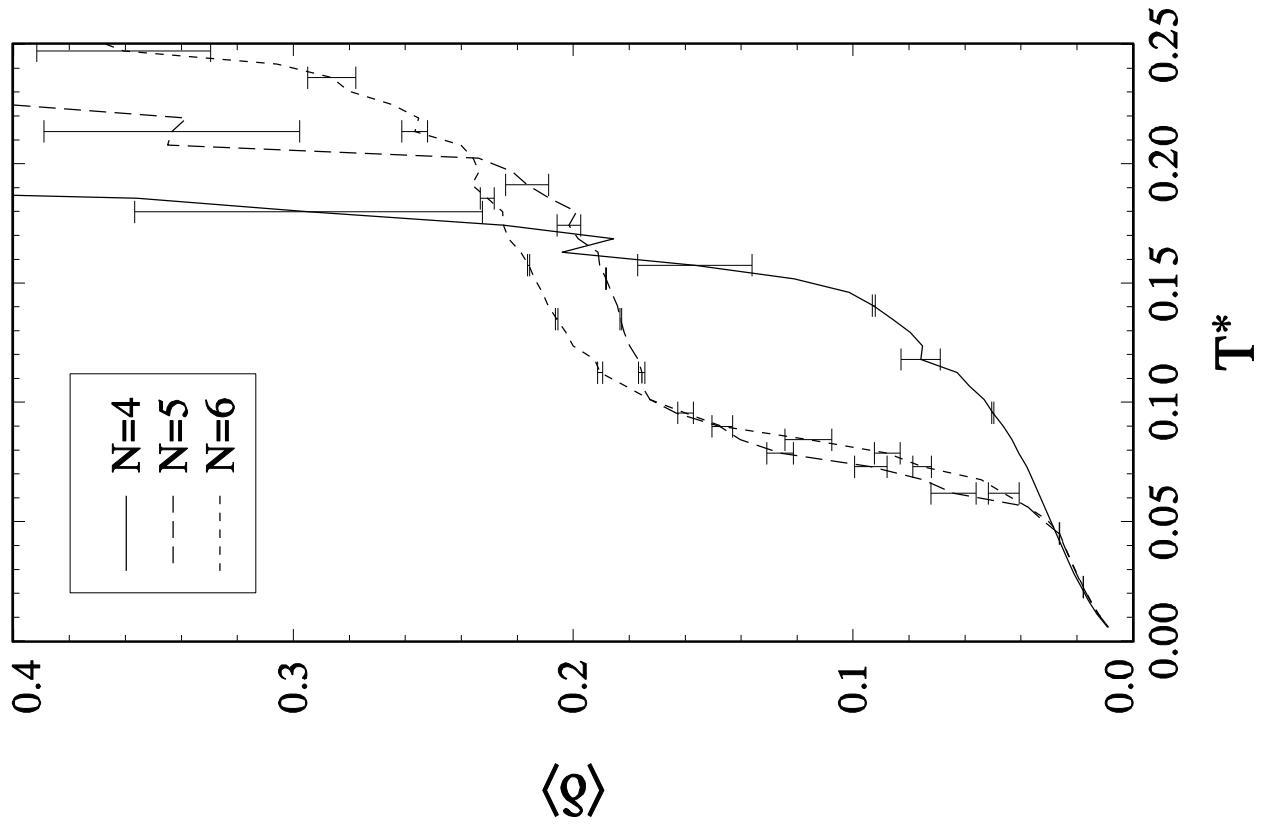




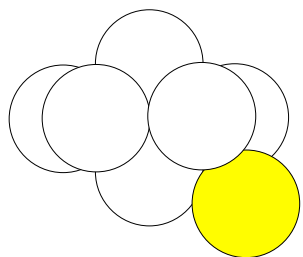




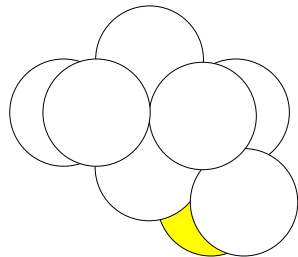




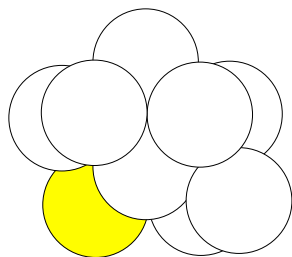
8



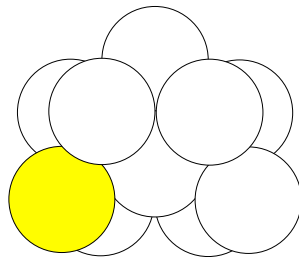
9



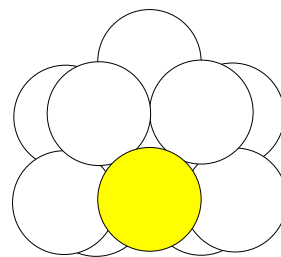
10



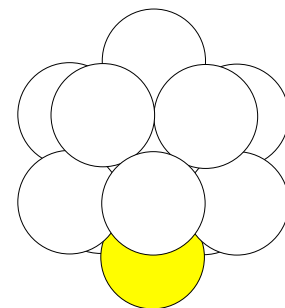
11



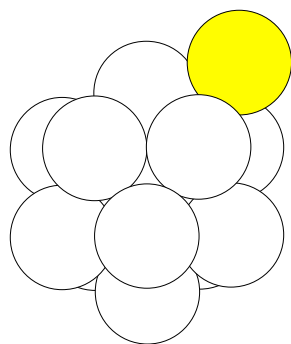
12



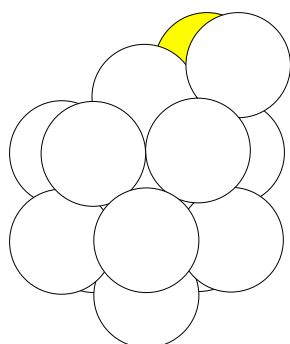
13



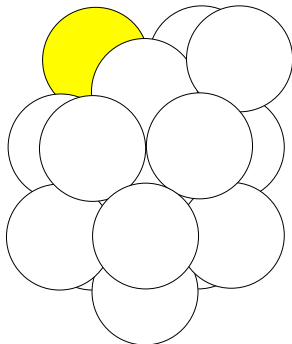
14



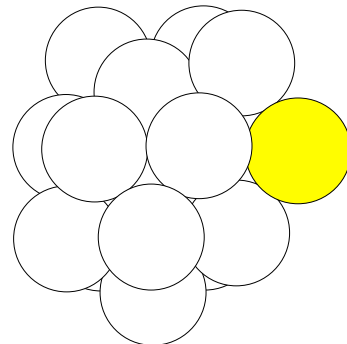
15



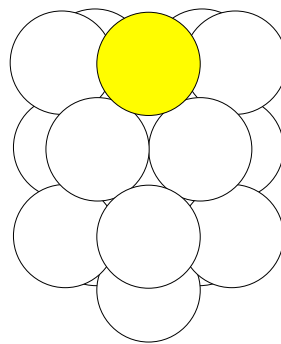
16



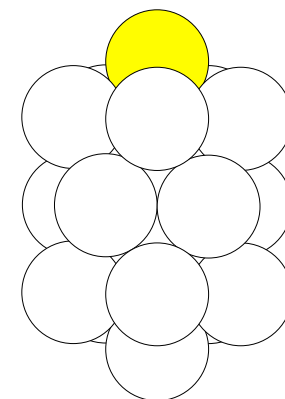
17

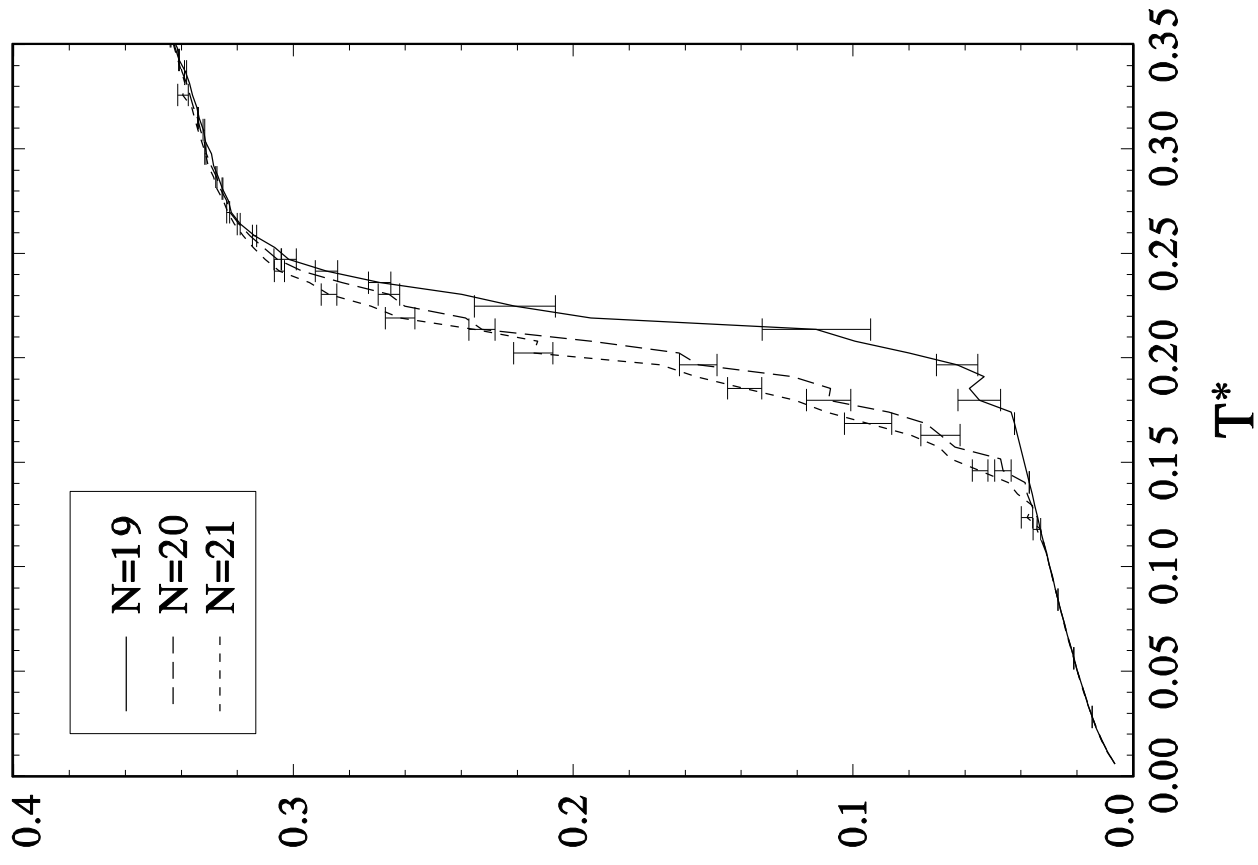
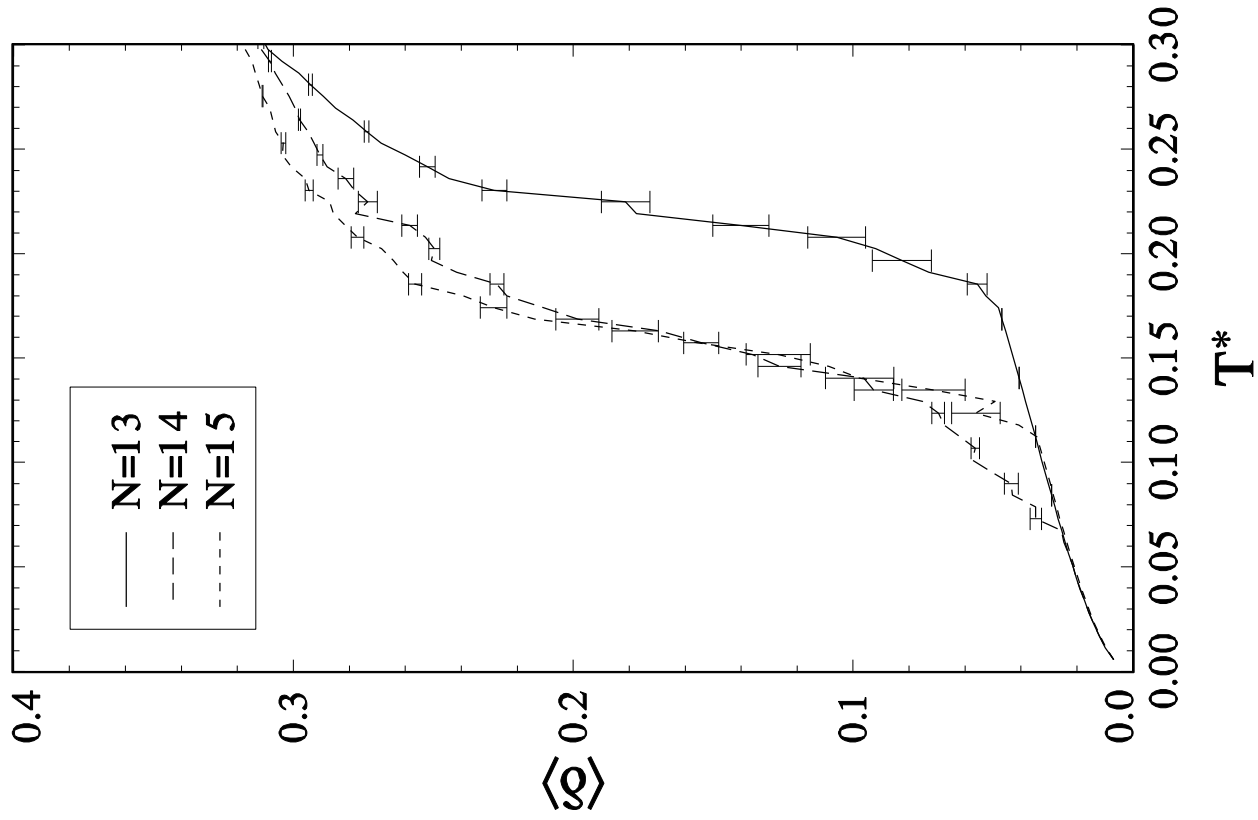


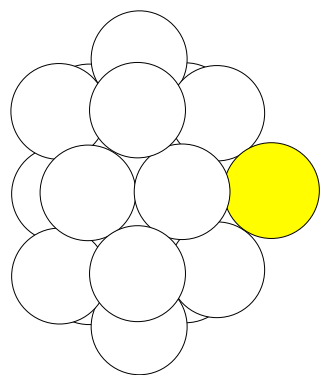
18



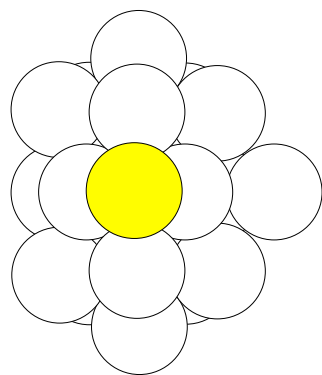
19



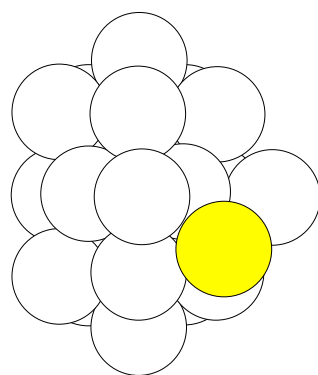




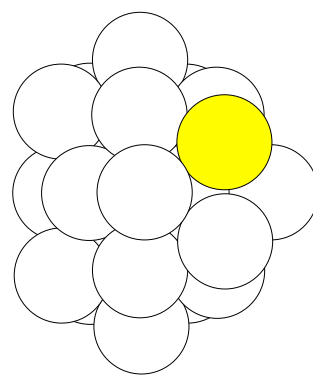
20



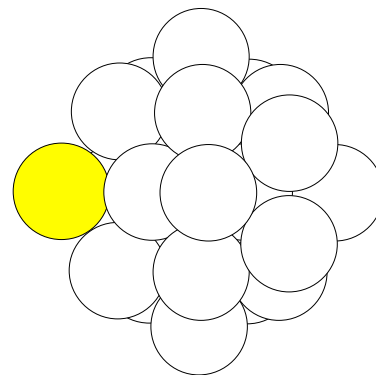
21



22



23



24

